

Synthesis of Ti_3AuC_2 , $\text{Ti}_3\text{Au}_2\text{C}_2$ and Ti_3IrC_2 by noble metal substitution reaction in Ti_3SiC_2 for high-temperature-stable Ohmic contacts to SiC

Hossein Fashandi, Martin Dahlgqvist, Jun Lu, Justinas Palisaitis, Sergey Simak, Igor Abrikosov, Johanna Rosén, Lars Hultman, Mike Andersson, Anita Lloyd Spetz and Per Eklund

The self-archived version of this journal article is available at Linköping University Institutional Repository (DiVA):

<http://urn.kb.se/resolve?urn=urn:nbn:se:liu:diva-139912>

N.B.: When citing this work, cite the original publication.

Fashandi, H., Dahlgqvist, M., Lu, J., Palisaitis, J., Simak, S., Abrikosov, I., Rosén, J., Hultman, L., Andersson, M., Lloyd Spetz, A., Eklund, P., (2017), Synthesis of Ti_3AuC_2 , $\text{Ti}_3\text{Au}_2\text{C}_2$ and Ti_3IrC_2 by noble metal substitution reaction in Ti_3SiC_2 for high-temperature-stable Ohmic contacts to SiC, *Nature Materials*, 16(8), 814-818. <https://doi.org/10.1038/NMAT4896>

Original publication available at:

<https://doi.org/10.1038/NMAT4896>

Copyright: Nature Publishing Group

<http://www.nature.com/>



1 Synthesis of Ti_3AuC_2 , $Ti_3Au_2C_2$ and Ti_3IrC_2 by noble-metal
2 substitution reaction in Ti_3SiC_2 for high-temperature-stable ohmic
3 contacts to SiC

4
5 Hossein Fashandi, Martin Dahlgqvist, Jun Lu, Justinas Palisaitis, Sergei I. Simak,
6 Igor A. Abrikosov, Johanna Rosen, Lars Hultman, Mike Andersson*, Anita
7 Lloyd Spetz*, and Per Eklund*

8
9 Department of Physics, Chemistry, and Biology (IFM), Linköping University, SE-581 83
10 Linköping, Sweden

11
12 KEYWORDS: Layered phases, noble metals, MAX phase ohmic contacts, oxidation
13 resistance

14
15
16
17
18
19
20
21
22
23
24
25
26
27
28 * Corresponding authors. E-mail:
29 perek@ifm.liu.se (P. Eklund)
30 spetz@ifm.liu.se (A. Lloyd-Spetz)
31 mikan@ifm.liu.se

(M.

Andersson)

32 **The large class of layered ceramics encompasses both van der Waals (vdW) and non-**
33 **vdW solids. While intercalation of noble metals in vdW solids is known, formation of**
34 **compounds by incorporation of noble-metal layers in non-vdW layered solids is largely**
35 **unexplored. Here, we show formation of Ti_3AuC_2 and $Ti_3Au_2C_2$ phases with up to 31%**
36 **lattice swelling by a substitutional solid-state reaction of Au into Ti_3SiC_2 single-crystal**
37 **thin films with simultaneous out-diffusion of Si. Ti_3IrC_2 is subsequently produced by a**
38 **substitution reaction of Ir for Au in $Ti_3Au_2C_2$. These phases form ohmic electrical**
39 **contacts to SiC and remain stable after 1000 h of aging at 600 °C in air. The present**
40 **results, by combined analytical electron-microscopy and *ab-initio* calculations, open**
41 **avenues for processing of noble-metal-containing layered ceramics that have not been**
42 **synthesized from elemental sources, along with tunable properties such as stable**
43 **electrical contacts for high-temperature power electronics or gas sensors.**

44

45 $M_{n+1}AX_n$ phases are a family of inherently nanolaminated ternary ceramics with more than 70
46 members. In this notation, M is an early transition metal, A is an element from groups 12–16,
47 X is carbon or nitrogen, and $n = 1-3$ and possibly higher^{1,2}. Structurally, they consist of
48 $M_{n+1}X_n$ sheets sandwiched in between one-atom-thick A-layers. The latter can be wet-
49 chemically removed or thermally desorbed from a $M_{n+1}AX_n$ phase resulting in the formation
50 of two-dimensional (2D) $M_{n+1}X_n$ sheets known as MXene^{3,4}. MXenes are a novel class of 2D
51 materials⁵⁻⁸ that are both hydrophilic and conductive, exhibit high volumetric capacitance^{9,10},
52 and allow for intercalation of a range of species^{11,12}. The intercalant then resides in the
53 lamellar voids between MXene layers. This is in contrast to their parent $M_{n+1}AX_n$ phases and
54 motivates the present study for synthesizing noble-metal-containing layered ceramics by an
55 ordered replacement of the A-layer crystal planes; from Si-planes to Au-, Au_2 - or Ir-planes.
56 Generally, $M_{n+1}AX_n$ phases possess a mixed nature of metal/ceramic properties as resistance
57 to wear and thermal shock, together with high thermal and electrical conductivities which
58 make them viable candidate materials for harsh-environment applications such as ohmic
59 contacts for high-temperature semiconductor electronics². For such applications, however,
60 high-temperature-induced surface oxidation and destructive interdiffusion between adjacent
61 metallic phases forming the contacts are the main reasons for failure¹³. Replacement of the A-
62 layer with noble metals to form *e.g.*, Ti_3AuC_2 can thus potentially modify $M_{n+1}AX_n$ phases to
63 withstand harsh oxidizing environments.

64

65 Here, we report substitution of Au and Ir in thin films of the $M_{n+1}AX_n$ phase Ti_3SiC_2 through
66 solid-state diffusion processes at ~650 °C. Fully replacing Si with Au, we show the synthesis
67 of the novel phases Ti_3AuC_2 , and $Ti_3Au_2C_2$ as well as Ti_3IrC_2 by replacing Au with Ir in
68 $Ti_3Au_2C_2$. These phases exhibit long-term high-temperature structural stability without Au
69 out-diffusion, as well as ohmicity to silicon carbide (SiC), yielding high-temperature-
70 compatible SiC ohmic contacts. Based on Ti_3AuC_2 and an oxygen-barrier capping layer of
71 Au/Iridium oxide (IrO_x) we designed an ohmic contact which survived a 1000-h annealing at
72 600 °C room-air with intact ohmicity and structure. These results have broad implications
73 since they demonstrate the ability to selectively replace the A layers with noble metals in
74 layered transition metal carbides.

75

76 Initially, 60-nm-thick ohmic Ti_3SiC_2 films were grown on 4H-SiC by a single-step growth
77 method, which is based on concurrent solid state reaction of sputter deposited Ti on SiC¹⁴.
78 Next, we sputter-deposited 200 nm of Au on the surface of Ti_3SiC_2 , as schematically

79 illustrated in Figure 1(a). Figure 1(b) is a scanning transmission electron microscopy (STEM)
80 image from the Ti_3SiC_2 layer of this sample showing M_3X_2 (Ti_3C_2) sheets separated by A-
81 layers (Si), typical of M_3AX_2 phases². The Au-covered Ti_3SiC_2 samples were then annealed
82 for 12 h at 670 °C in N_2 gas atmosphere to avoid oxidation. Figure 1 (c) is an STEM image of
83 the same sample, after the annealing procedure, at the region where Ti_3SiC_2 was initially
84 present. The brightness of a species in STEM is proportional to its mass. The A-layers
85 separating the Ti_3C_2 sheets in Figure 1(c) are much brighter than Si planes in Figure 1 (b) and
86 are thus composed of the much heavier element Au, which has diffused in between the Ti_3C_2
87 sheets of Ti_3SiC_2 . Figure 1(d) is an energy dispersive X-ray spectroscopy (EDX) line-scan of
88 Ti-K α and Au-M α signals along the arrow in Figure 1(c). The maximum of one elemental
89 signal matches the minimum of the other, unambiguously identifying the inserted element in
90 Ti_3SiC_2 as Au. Regions of the Ti_3SiC_2 layer close to the substrate and thus far from the Au
91 source exhibit incomplete Au layers. Figure 1(e) is a STEM image and the related EDX map
92 from such a location, showing that there is a distinct reaction front advancing step-wise over
93 layers into the Ti_3SiC_2 . Refer to the supplementary material for a STEM movie (described in
94 Supplementary text section S.14) showing the process *in situ*.

95
96 The Si was found to have diffused out of the annealed Ti_3SiC_2 using scanning electron
97 microscopy (SEM)/EDX, (see S1). A high oxygen content of the Si-rich regions and the fact
98 that no X-ray diffraction (XRD) peaks related to Si-containing phases were observed in the
99 annealed samples, indicate the formation of amorphous SiO_2 on the sample surfaces while
100 they were stored in room-air after the annealing procedure and prior to the SEM/EDX study.
101 The Si content of the A layers in the novel structure is negligible, based on EDX results, and
102 it can thus be described as Ti_3AuC_2 . Figures 1(f) and 1(g) show STEM of Ti_3AuC_2 with the
103 beam aligned along the two zone axes $[11\bar{2}0]$ and $[1\bar{1}00]$, respectively. The atomic positions
104 match those of a M_3AX_2 phase. Figure 1(h) shows X-ray diffractograms of the sample
105 illustrated in Figure 1(a) before and after the annealing. The 0001 peaks of Ti_3SiC_2 have
106 shifted towards lower angles as a result of the Au insertion with its larger atomic size. The
107 intercalation thus results in an increased *c* lattice parameter from 17.63 Å for Ti_3SiC_2 to 18.56
108 Å in Ti_3AuC_2 , i.e., by 5.3%. The residual peaks of Ti_3SiC_2 could be further removed by
109 annealing at higher temperatures, e.g., at 700 °C, see S4. Ti_3AuC_2 with the space group of
110 $\text{P6}_3/\text{mmc}$ (194) has the same crystal structure as Ti_3SiC_2 .

111
112 With density functional theory (DFT), we studied the formation enthalpy of the Ti_3AuC_2
113 phase by comparing its 0-K energy to the most competing phases in Ti-Au-C system, (see S2
114 for the computations). Included competing phases are based on experimental phase diagrams
115 and what is present in similar systems, see S3 and S6. These calculations showed that
116 Ti_3AuC_2 has negative formation enthalpy when compared to the most competing phases,
117 indicating its thermodynamic stability. Furthermore, the simulated phonon frequencies are
118 positive, i.e., the phase is dynamically stable, see S7.

119
120 Using the same non-annealed Au/ Ti_3SiC_2 films on SiC, we deposited ~700 nm of Ir on Au, as
121 illustrated in Figure 2(a). Ir deposition was made thick enough to isolate the sample from the
122 ambient since Au (unlike Ir) is prone to recrystallization, forming grain boundaries, which can
123 facilitate interdiffusion of gas species. Annealing at 600 °C for 12 h and in N_2 atmosphere
124 resulted in the A-layers becoming filled with double layers of Au, as can be seen in Figure

125 2(b), with a resultant 31 % increase of the c lattice parameter. This is a remarkable extension
126 of the results of single-layer replacement for Au/Ti₃SiC₂/SiC samples (Fig. 1(a)). Figure 2(c)
127 shows a STEM/EDX image that reveals locations with different number of Au layers
128 including the transition between regular two-atomic-layer Au (top part) and forking between
129 two and three atomic Au layers (mid-section) as well as double-to-triple-layer Au (lower
130 part), resulting in continued swelling in the c direction. Such features can be a result of
131 stacking faults in the original Ti₃SiC₂ host (See S.11).

132

133 Figure 2(d) shows the STEM image of this phase along the $[11\bar{2}0]$ direction. The Ti₃C₂ sheets
134 are located in a zig-zag pattern along the c axis, and notably not mirrored with respect to the
135 A-layers as is the case in Ti₃AuC₂ and M₃AX₂ phases. Each two-atom-thick A-layer is
136 composed of two mono-layers of Au with different in-plane positions. This is a different
137 crystal structure from the only known M_{n+1}A₂X_n phase to-date (Mo₂Ga₂C) in which the two
138 monolayers of Ga forming each A-layer are located directly on top of each other^{15,16}.
139 Moreover, the A-layers in Ti₃Au₂C₂ are located in a zigzag-zagzag pattern along the c axis,
140 which is also visible in Figure 2(b) in a wider view. Figure 2(e) is a STEM image along the
141 $[1\bar{1}00]$ direction showing the same positions for all the atoms in each column. Negligible Si-
142 content within the Au-containing regions was determined using EDX. Based on the above-
143 mentioned characteristics, we assumed a unit cell within the P-3m1 space group, as illustrated
144 in Figure 2(f). Figure 2(g) shows X-ray diffractograms of the sample in Figure 2(a) before and
145 after the annealing procedure showing the c lattice parameter of Ti₃Au₂C₂ to be $23.14 \times 2 =$
146 46.28 \AA (31 % lattice swelling). *Ab-initio* simulations based on the structure in Figure 2(f)
147 show negative formation enthalpy for this phase (see S3 and S6) as well as dynamic stability
148 (see section S7), thus supporting the determined crystal structure.

149

150 Both Ti₃AuC₂ and Ti₃Au₂C₂ phases showed ohmic behavior on SiC, as characterized by
151 current/voltage (I/V) measurements¹⁴ on two separated contact areas ($\approx 3\text{mm} \times 8\text{mm}$) using
152 two removable probes. In order to investigate the functionality of these structures as high-
153 temperature ohmic contacts, we investigated aging at 600 °C. The Au/Ti₃AuC₂/SiC sample
154 remained intact in nitrogen atmosphere for 100 h. However, when annealed in air, this sample
155 completely transformed into Ti₃Au₂C₂ within the first 20 h, as confirmed by XRD. After 60 h,
156 the diffraction peaks disappeared due to oxidation into X-ray amorphous phases. We aged the
157 Ir-capped sample depicted in Figure 2(a) for 1000 h in air. Figure 3 (a) is a low resolution
158 STEM image of the sample after the 1000-h experiment. As can be seen, the Au layer has
159 diffused through Ir forming a $\approx 200 \text{ nm}$ thick layer. Figure 3 (b) is a STEM image of the
160 initial Ti₃SiC₂ site after the 1000-h anneal. This site (see above) had completely transformed
161 into Ti₃Au₂C₂ after 12 h of annealing. However, Figure 3 (b) shows that the A layers are filled
162 with monolayers of a heavy metal, instead of double layers. The corresponding EDX in
163 Figure 3 (c) shows them to be composed of Ir with negligible Au content, thus resulting in yet
164 another phase: Ti₃IrC₂. Based on STEM results, the structure of Ti₃IrC₂ is identical to the
165 regular M₃AC₂ structure. DFT results (see S5), further shows that structure has positive
166 formation enthalpy with respect to the most competing phases and exhibits positive phonon
167 frequencies. These findings suggest that Ti₃IrC₂ is a metastable M_{n+1}AX_n phase. This is
168 further supported by our attempt to synthesize Ti₃IrC₂ through a direct intercalation of Ir into
169 Ti₃SiC₂, where a 200-nm-thick Ir layer was deposited directly on Ti₃SiC₂ film grown on SiC,
170 whereafter the sample was annealed for 100 h at 600 °C. In that case, the annealing process
171 destroyed both the ohmicity and the layered structure of Ti₃SiC₂ forming nanocrystalline Ti-
172 and Ir-containing intermetallic phases. Electron energy loss spectroscopy of the Au and Ir

173 showed no indication of any difference in bonding when compared to those of pure elemental
174 cases (see S.12). These findings indicate a zero (or near-zero) valence state for the noble
175 metals whose bonding state are seemingly of covalent/metallic nature. Note that this should
176 not be confused with the intercalation of zerovalent atoms in van der Waals solids.¹⁷⁻¹⁹

177

178 The ohmicity of the contact remained intact by transformation from $\text{Ti}_3\text{Au}_2\text{C}_2$ to Ti_3IrC_2
179 during the 1000 h experiment. However, migration of the Au layer towards the surface
180 potentially leaves voids affecting the structural stability¹³ (see S.9). To overcome this, we used
181 IrO_x ²⁰ films instead of Ir (for a high electrical conductivity phase that eliminates surface
182 oxidation as a cause of failure) on Au-covered Ti_3SiC_2 , see Figure 4 (a). We annealed the
183 sample for 1000 h in ambient air. The annealing resulted in insertion of single-layer Au in the
184 Ti_3SiC_2 forming Ti_3AuC_2 . Figure 4 (b) shows an STEM image of such a sample after
185 annealing for 1000 h at 600 °C and in ambient air. As can be seen, the $\text{Ti}_3\text{AuC}_2/\text{Au}$ stack has
186 remained intact, showing that this design is stable. Figure 4 (c) is the I/V curve after the 1000
187 h annealing experiment, showing a retained linear characteristic of ohmic contacts. A contact
188 with the use of IrO_x directly on $\text{Ti}_3\text{SiC}_2/\text{SiC}$ as an oxygen barrier lasts for less than 100 h at
189 600 °C air as observed by I/V and XRD (see S.10).

190

191 In order to explain the massive replacement of Si with Au in Ti_3SiC_2 , we recall that Au
192 induces instability in the bonding character of the Si adjacent to the Au in Au-Si diffusion
193 couples by screening of the Coulomb interaction by its free electrons.²¹ In bulk, the Au-Si
194 system forms a deep eutectic at 363 °C, well below our annealing temperature. A liquid phase
195 is present throughout the entire phase diagram with no solid silicide phases. Au and Si have
196 no mutual solubility in the solid state while Si surface-segregation in Au-Si alloys, or in Au-
197 covered Si substrates, is also known.^{22,23} Si atoms are loosely bonded to Ti_3SiC_2 as a general
198 trend in $\text{M}_{n+1}\text{AX}_n$ phases. At 600 °C and in the presence of Au reservoir surrounding the
199 Ti_3SiC_2 grains as the primarily most possible diffusion path, the loosely bonded Si atoms find
200 a lower chemical potential diffusing in Au. The presence of stacking faults in Ti_3SiC_2 can
201 likely accelerate the diffusion. This leaves the A-layers vacant which in turn are back-filled
202 with Au atoms, while appreciating volume constraints for diffusion on the A-layers imposed
203 by the present Ti_3SiC_2 films. The above-mentioned factors are also consistent with the fact
204 that Ti_3IrC_2 could not be formed here by annealing Ir/ $\text{Ti}_3\text{SiC}_2/\text{SiC}$ samples at 600 °C. At this
205 temperature, the entire Ir-Si phase diagram consists of several solid silicide phases which
206 formation seemingly hinders the out-diffusion of Si.²⁴ For the case of successful Ir in-
207 diffusion in $\text{Ti}_3\text{Au}_2\text{C}_2$, Au and Ir exhibit very little mutual solubility while forming no
208 compounds possibly able of blocking the diffusion process.²⁵ Moreover, surface segregation
209 of Au in Au-Ir alloys is also expected.²⁶ Based on these while taking into account the high
210 diffusivity of Au, the synthesis of Ti_3IrC_2 can be explained.

211

212 The remarkable stability of the Ti_3AuC_2 ohmic contact to SiC stands out. SiC is a preferred
213 choice for high temperature electronics based on its highly stable electronic and structural
214 properties at elevated temperature^{27,28}. Yet, the degradation of the metallic ohmic contacts
215 needs to be overcome¹³ in order for it to find its path into high-temperature industrial
216 applications, *e.g.*, *in situ* chemical gas sensors for exhaust monitoring of vehicles²⁹. Other
217 reports at similar conditions to our aging experiments show complete degradation of the
218 contact at considerably less thermal loading and period^{30,31}.

219

220 In conclusion, we have discovered the layered Ti_3AuC_2 , $\text{Ti}_3\text{Au}_2\text{C}_2$, and Ti_3IrC_2 phases by
221 ordered noble-metal exchange of A-layers in nanolaminated transition metal carbides,
222 $\text{M}_{n+1}\text{AX}_n$ phases. The formation mechanism and the resulting phases are structurally and
223 reaction-wise different to intercalation of other species into Si- or Al-depleted two-
224 dimensional MXene phases^{11,12}, which host the intercalation species inside the laminar voids
225 in between their layers. Here, the reaction takes place through an ordered exchange on
226 specific crystal planes, with Au planes substituting for Si and Ir for double-Au planes,
227 respectively. These results constitute a starting point for exploration of what is likely to be a
228 large family of noble-metal-containing transition-metal carbides/nitrides. Also, they offer
229 prospects and means for property tailoring in nanolaminated functional ceramics, as
230 demonstrated here for high-temperature ohmicity with corresponding implications for
231 enhanced electrical or magnetic properties.

232 METHODS

233

234 The depositions were performed using 4 ° off-axis n-type 4H-SiC substrates with $\sim 10^{18} \text{ cm}^{-3}$
235 of carrier concentration and 10×10 mm in size. The growth and characterization method for
236 Ti_3SiC_2 ohmic contacts was described elsewhere¹⁴. For the synthesis of Au and Ir layers, the
237 samples were transferred (ex situ) into a second ultra-high vacuum stainless steel sputtering
238 chamber, equipped with 4 magnetrons placed 20 cm above the substrate surface, each at 20 °
239 off the substrate normal, with the base pressure lower than 10^{-8} Pa obtained by a 550 l/s turbo
240 molecular pump backed by a rotary vane pump. Prior to the depositions, the surface of the
241 Ti_3SiC_2 Ohmic contacts were cleaned by a 5-second dip in buffered HF (NH_3F (25 gr) +
242 H_2O (50 ml) + HF (10 ml)) to remove any surface oxide followed by a thorough rinse in
243 distilled water, blow-dried in N_2 and inserted into the load-lock of the deposition system. All
244 sputtering targets were 2 inches in diameter with the purity of 99.99% or higher. Ar was used
245 as the sputtering gas with the constant pressure of 1.8 mtorr. For the growth of IrO_x , (see S8).
246 25% of partial pressure of O_2/Ar was used for sputtering. All the sputter-depositions were in
247 DC mode with the current (mA) and voltages (V) of [(520), (420)]_{Ir}, [(240), (440)]_{Au}, [(250),
248 (570)]_{IrO_x} which yielded the deposition rates of $r_{\text{Ir}} = 350 \text{ \AA/s}$, $r_{\text{Au}} = 260 \text{ \AA/s}$, and $r_{\text{IrO}_x} = 350$
249 \AA/s obtained using scanning electron microscopy (SEM) for cross-sectional samples. All the
250 depositions were performed with floating substrate bias and at room temperature. The reason
251 for the low temperature was to obtain a fine-grained microstructure and avoid columnar
252 growth and the consequent column boundaries which can act as oxygen diffusion paths. X-ray
253 diffraction (XRD) was performed using a Philips PW 1820 instrument (Cu ($K\alpha$), θ -2 θ scan,
254 aligned with the substrate (0001) peak). SEM was performed in a LEO 1550 for film
255 thickness measurement via cross-sectional samples and surface imaging. Transmission
256 electron microscopy (TEM) was performed in the Linköping monochromated double-
257 spherical-aberration-corrected FEI Titan3 60–300 operated at 300 kV, equipped with the
258 SuperX EDX system. Cross-sectional samples were first mechanically polished to a thickness
259 of about 50 μm , followed by ion-beam milling with Ar^+ in a Gatan precision ion polishing
260 system (PIPS) at 5 keV with a final polishing step at 1 keV of ion energies. The annealing
261 procedure was performed in a cylindrical ceramic oven, exposed to ambient air, in which the
262 sample is placed at its center. The temperature was controlled simultaneously during the
263 whole experiments using a thermocouple at the sample position. The temperature of the oven
264 was raised with the ramp of 17.6 °C /min to the annealing temperature of 650 °C.

265

266

267 ACKNOWLEDGMENTS

268 We acknowledge Dr. Henrik Pedersen for useful discussions about the results. We
269 acknowledge the support from the VINN Excellence Center in research and innovation on
270 Functional Nanoscale Materials (FunMat) by the Swedish Governmental Agency for
271 Innovation Systems (VINNOVA) and the Swedish Government Strategic Research Areas in
272 Materials Science on Functional Materials at Linköping University (Faculty Grant SFO-Mat-
273 LiU No. 2009 00971). P.E, J.L., M.D., and J.R. also acknowledge support from the Swedish
274 Foundation for Strategic Research through the Future Research Leaders 5 Program and the
275 Synergy Grant FUNCASE, Functional Carbides and Advanced Surface Engineering. I.A.A. is
276 grateful to support provided by the e-Science Research Centre (SeRC). P. E. also
277 acknowledges support from the European Research Council under the European
278 Community's Seventh Framework Programme (FP/2007-2013) / ERC grant agreement no

279 335383. L.H. acknowledges the Knut and Alice Wallenberg Foundation for a Scholar Grant
280 and support to the Linköping Ultra Electron Microscopy Laboratory. The calculations were
281 performed on resources provided by the Swedish National Infrastructure for Computing
282 (SNIC) at National Supercomputer Centre (NSC) and PDC.

283

284 ADDITIONAL INFORMATION

285 Supplementary information is available in the online version of the paper. Correspondence
286 and requests for materials should be addressed to M. A., A.L.S, and P.E.

287

288 DATA AVAILABILITY STATEMENT

289 Essential all data generated or analyzed during this study are included in this published article
290 (and its supplementary information files). The datasets (computational data and source data
291 for graphs) generated during and/or analyzed during the current study are available in the
292 Zenodo repository at <https://doi.org/10.5281/zenodo.376969>.

293

294

295 COMPETING FINANCIAL INTERESTS

296 The authors declare no competing financial interests.

297

298 AUTHOR CONTRIBUTIONS

299 H.F, M. A., A. L.-S., and P. E. conceived and initiated the work. H. F. conducted and
300 analyzed the growth, annealing, XRD, and SEM. M.D. performed the *ab initio* studies with
301 input from S. I. S., I. A.A., J. R., H.F., and P.E.

302 J.L. conducted the STEM and EDX and analyzed the results with contributions from H.F.,
303 L.H and P.E.

304 J. P. designed, executed, and interpreted the *in-situ* annealing in TEM, and recorded the
305 movie.

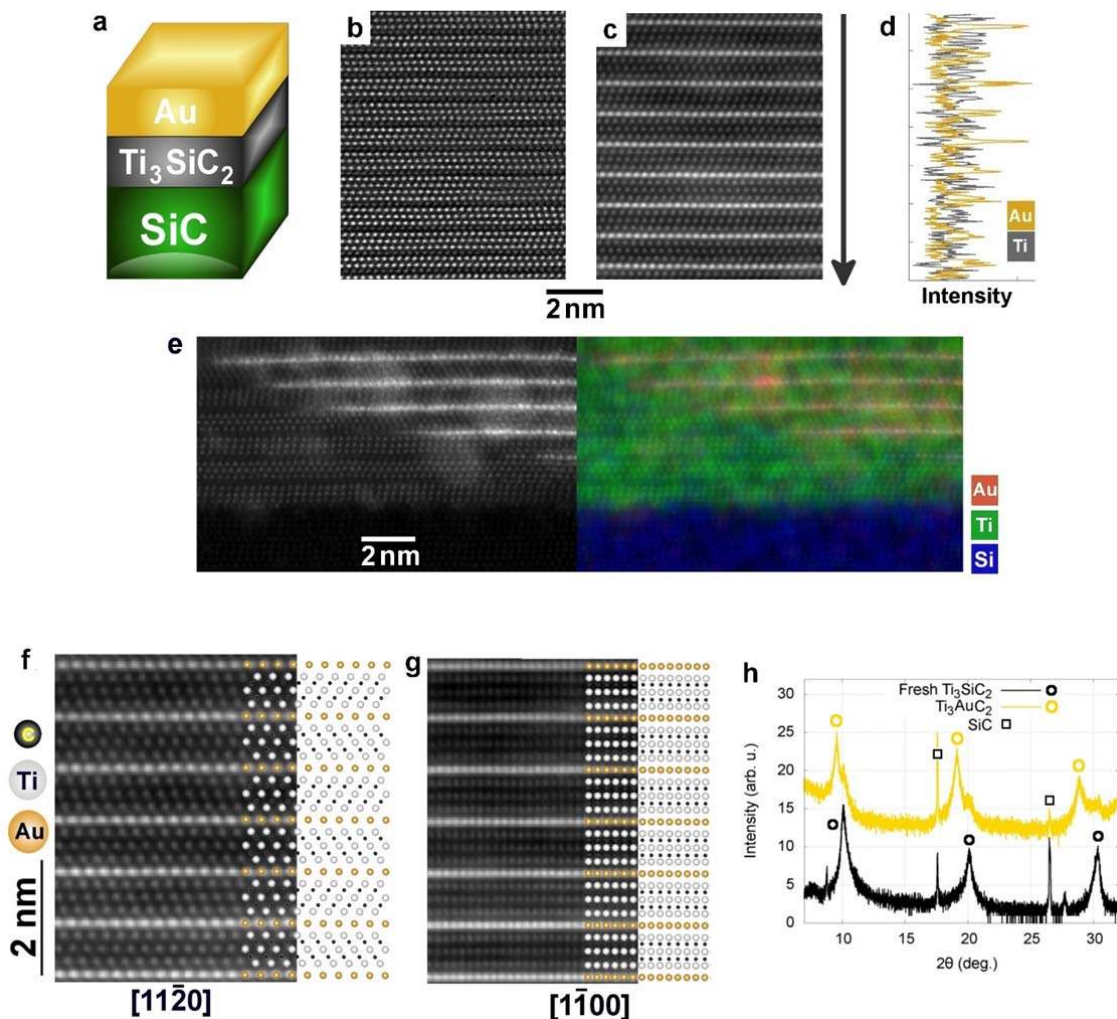
306 H.F., M.D., and P.E. wrote the manuscript with contributions from the other coauthors. All
307 coauthors read and commented on successive drafts of the manuscript.

308 M. A., A. L.-S., and P.E. supervised the work.

309 REFERENCES

- 310 1. Barsoum, M. W. & Radovic, M. Elastic and Mechanical Properties of the MAX Phases. *Annu.*
311 *Rev. Mater. Res.* **41**, 195–227 (2011).
- 312 2. Eklund, P., Beckers, M., Jansson, U., Högberg, H. & Hultman, L. The $M_{n+1}AX_n$ phases:
313 Materials science and thin-film processing. *Thin Solid Films* **518**, 1851–1878 (2010).
- 314 3. Naguib, M., Mochalin, V. N., Barsoum, M. W. & Gogotsi, Y. 25th anniversary article:
315 MXenes: a new family of two-dimensional materials. *Adv. Mater.* **26**, 992–1005 (2014).
- 316 4. Naguib, M. *et al.* Two-dimensional nanocrystals produced by exfoliation of Ti_3AlC_2 . *Adv.*
317 *Mater.* **23**, 4248–53 (2011).
- 318 5. Halim, J. *et al.* Synthesis and Characterization of 2D Molybdenum Carbide (MXene). *Adv.*
319 *Funct. Mater.* **26**, 3118–3127 (2016).
- 320 6. Dillon, A. D. *et al.* Highly Conductive Optical Quality Solution-Processed Films of 2D
321 Titanium Carbide. *Adv. Funct. Mater.* **26**, 3118–3127 (2016).
- 322 7. Urbankowski, P. *et al.* Synthesis of two-dimensional titanium nitride Ti_4N_3 (MXene).
323 *Nanoscale* **8**, 11385–11391 (2016).
- 324 8. Zhou, J. *et al.* A Two-Dimensional Zirconium Carbide by Selective Etching of Al_3C_3 from
325 Nanolaminated $Zr_3Al_3C_5$. *Angew. Chem. Int. Ed.* **55**, 5008–5013 (2016).
- 326 9. Ghidui, M., Lukatskaya, M. R., Zhao, M.-Q., Gogotsi, Y. & Barsoum, M. W. Conductive two-
327 dimensional titanium carbide ‘clay’ with high volumetric capacitance. *Nature* **516**, 78–81
328 (2014).
- 329 10. Ling, Z. *et al.* Flexible and conductive MXene films and nanocomposites with high
330 capacitance. *Proc. Natl. Acad. Sci. U. S. A.* **111**, 16676–81 (2014).
- 331 11. Lukatskaya, M. R. *et al.* Cation intercalation and high volumetric capacitance of two-
332 dimensional titanium carbide. *Science* **341**, 1502–5 (2013).
- 333 12. Mashtalir, O. *et al.* Intercalation and delamination of layered carbides and carbonitrides. *Nat.*
334 *Commun.* **4**, 1716 (2013).
- 335 13. Wang, Z., Liu, W. & Wang, C. Recent Progress in Ohmic Contacts to Silicon Carbide for
336 High-Temperature Applications. *J. Electron. Mater.* **45**, 267–284 (2016)
- 337 14. Fashandi, H. *et al.* Single-step synthesis process of Ti_3SiC_2 ohmic contacts on 4H-SiC by
338 sputter-deposition of Ti. *Scr. Mater.* **99**, 53–56 (2015).
- 339 15. Lai, C.-C. *et al.* Structural and chemical determination of the new nanolaminated carbide
340 Mo_2Ga_2C from first principles and materials analysis. *Acta Mater.* **99**, 157–164 (2015).
- 341 16. Hu, C. *et al.* Mo_2Ga_2C : a new ternary nanolaminated carbide. *Chem. Commun. (Camb)*. **51**,
342 6560–3 (2015).
- 343 17. Koski, K. J. *et al.* High-density chemical intercalation of zero-valent copper into Bi_2Se_3
344 nanoribbons. *J. Am. Chem. Soc.* **134**, 7584–7 (2012).
- 345 18. Yao, J. *et al.* Optical transmission enhancement through chemically tuned two-dimensional
346 bismuth chalcogenide nanoplates. *Nat. Commun.* **5**, 5670 (2014).
- 347 19. Motter, J. P., Koski, K. J. & Cui, Y. General Strategy for Zero-Valent Intercalation into Two-
348 Dimensional Layered Nanomaterials. *Chem. Mater.* **26**, 2313–2317 (2014).
- 349 20. Trupina, L. *et al.* Iridium layer as oxygen barrier and growth substrate for oriented PZT thin
350 films. **9**, 1508–1510 (2007).
- 351 21. Tu, K. N. Selective growth of metal-rich silicide of near-noble metals. *Appl. Phys. Lett.* **27**, 221
352 (1975).
- 353 22. Hiraki, A. Formation of silicon oxide over gold layers on silicon substrates. *J. Appl. Phys.* **43**,
354 3643 (1972).

- 355 23. Lee, S., Stephens, J. A. & Hwang, G. S. On the Nature and Origin of Si Surface Segregation in
356 Amorphous AuSi Alloys. 3037–3041 (2010).
- 357 24. *Hg-Ho – La-Zr*. Madelung, O., Ed.; Landolt-Börnstein - Group IV Physical Chemistry;
358 Springer-Verlag: Berlin/Heidelberg, 1997; Vol. G.
- 359 25. *Ac-Au – Au-Zr*. Madelung, O., Ed.; Landolt-Börnstein - Group IV Physical Chemistry;
360 Springer-Verlag: Berlin/Heidelberg, 1991; Vol. A.
- 361 26. Ruban, A. V, Skriver, H. L. & No, J. K. Surface segregation energies in transition-metal alloys.
362 **59**, 990–1000 (1999).
- 363 27. Hedayati, R., Lanni, L., Rusu, A. & Zetterling, C.-M. Wide Temperature Range Integrated
364 Bandgap Voltage References in 4H–SiC. *IEEE Electron Device Lett.* **37**, 146–149 (2016).
- 365 28. Wijesundara, M. & Azevedo, R. *Silicon Carbide Microsystems for Harsh Environments*.
366 (Springer New York, 2011).
- 367 29. Andersson, M., Pearce, R. & Lloyd Spetz, A. New generation SiC based field effect transistor
368 gas sensors. *Sensors Actuators B Chem.* **179**, 95–106 (2013).
- 369 30. Daves, W., Krauss, A., Haublein, V., Bauer, A. J. & Frey, L. Structural and Reliability
370 Analysis of Ohmic Contacts to SiC with a Stable Protective Coating for Harsh Environment
371 Applications. *ECS J. Solid State Sci. Technol.* **1**, P23–P29 (2012).
- 372 31. Virshup, A. *et al.* Investigation of Thermal Stability and Degradation Mechanisms in Ni-Based
373 Ohmic Contacts to n-Type SiC for High-Temperature Gas Sensors. *J. Electron. Mater.* **38**,
374 569–573 (2009).
- 375

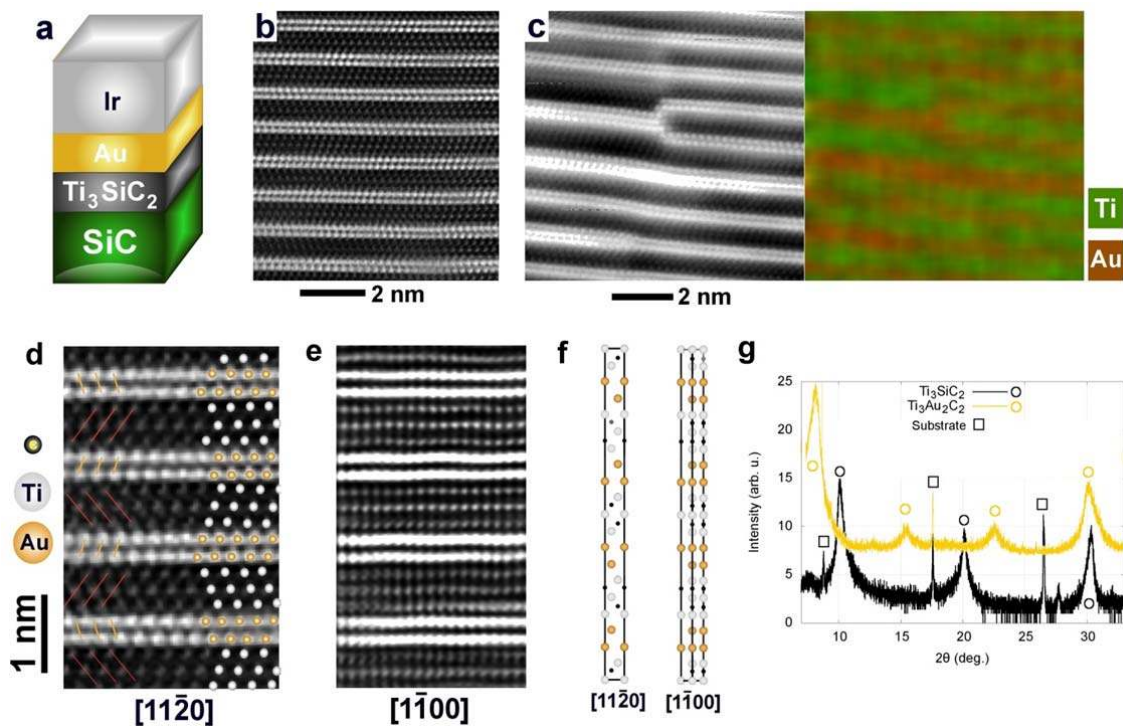


376

377 **Figure 1. Transformation from Ti_3SiC_2 to Ti_3AuC_2 .** (a) Schematic illustration of the gold-
 378 covered Ti_3SiC_2 layer on SiC prior to the reaction at 670 °C. (b) HR-STEM image of the
 379 Ti_3SiC_2 site of the sample illustrated in (a) prior to the annealing. (c) HR-STEM of Ti_3AuC_2
 380 phase formed between the SiC and the Au during the annealing. (d) EDX line-scan along the
 381 arrow depicted in (c) mapping Ti- $K\alpha$ and Au- $M\alpha$ signals. (e) HR-STEM and the
 382 corresponding EDX map of the annealed sample showing Au diffusing in between the Ti_3C_2
 383 layers. (f) and (g) Atomic positions of Ti_3AuC_2 from different orientations based on HR-
 384 STEM results. (h) 000l ($l=2, 4, \text{ and } 6$) peaks of the XRD patterns of Ti_3SiC_2 and Ti_3AuC_2
 385 before and after the annealing, respectively.

386

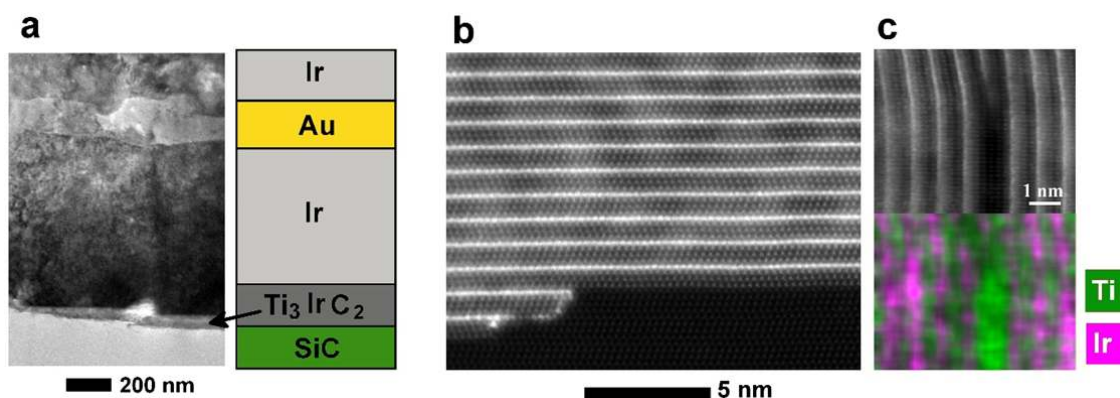
387



388

389 **Figure 2. Transformation from Ti_3SiC_2 to $\text{Ti}_3\text{Au}_2\text{C}_2$.** (a) Schematic illustration of the
 390 iridium- and gold-covered Ti_3SiC_2 layer on SiC prior to the reaction at 600 °C. (b) $\text{Ti}_3\text{Au}_2\text{C}_2$
 391 formed between the SiC and the Au during the annealing. (c) HR-STEM and corresponding
 392 EDX of Ti-K α and Au-M α signals showing stacking faults in $\text{Ti}_3\text{Au}_2\text{C}_2$. (d) Atomic positions
 393 and stacking orders of $\text{Ti}_3\text{Au}_2\text{C}_2$ based on HR-STEM along the $[11\bar{2}0]$ direction. (e) HR-
 394 STEM of atomic positions along $[1\bar{1}00]$. (f) Unit cell for $\text{Ti}_3\text{Au}_2\text{C}_2$ neglecting the disorders
 395 along the Au planes. (g) (0001) peaks in the X-ray diffractograms of Ti_3SiC_2 and $\text{Ti}_3\text{Au}_2\text{C}_2$.

396

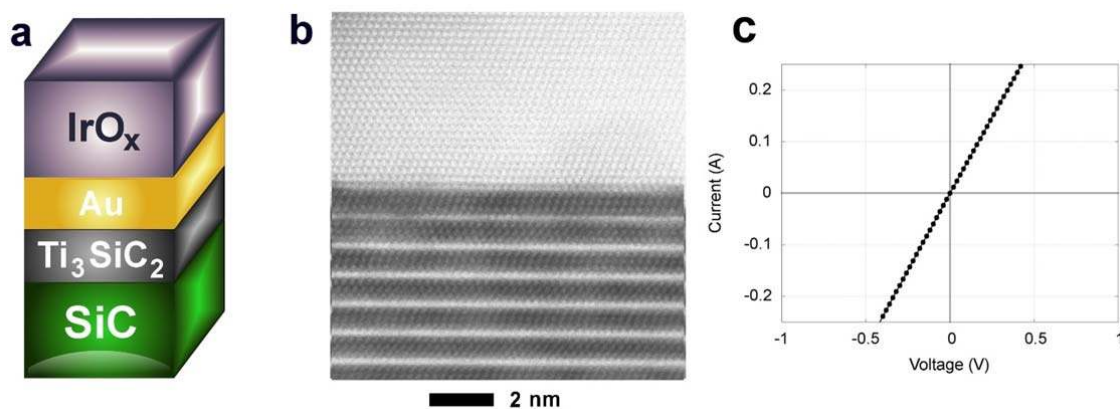


398

399 **Figure 3. Transformation from $\text{Ti}_3\text{Au}_2\text{C}_2$ to Ti_3IrC_2 by metal exchange.** (a) Low-
 400 resolution STEM of Ir/Au/ $\text{Ti}_3\text{Au}_2\text{C}_2$ /SiC sample annealed for 500 h in 600 °C along with the
 401 schematic illustration of the layers stacking change due to the annealing. (b) High resolution
 402 STEM of Ti_3IrC_2 . (c) Energy dispersive X-ray spectroscopy of Ti and Ir signals of Ti_3IrC_2 .

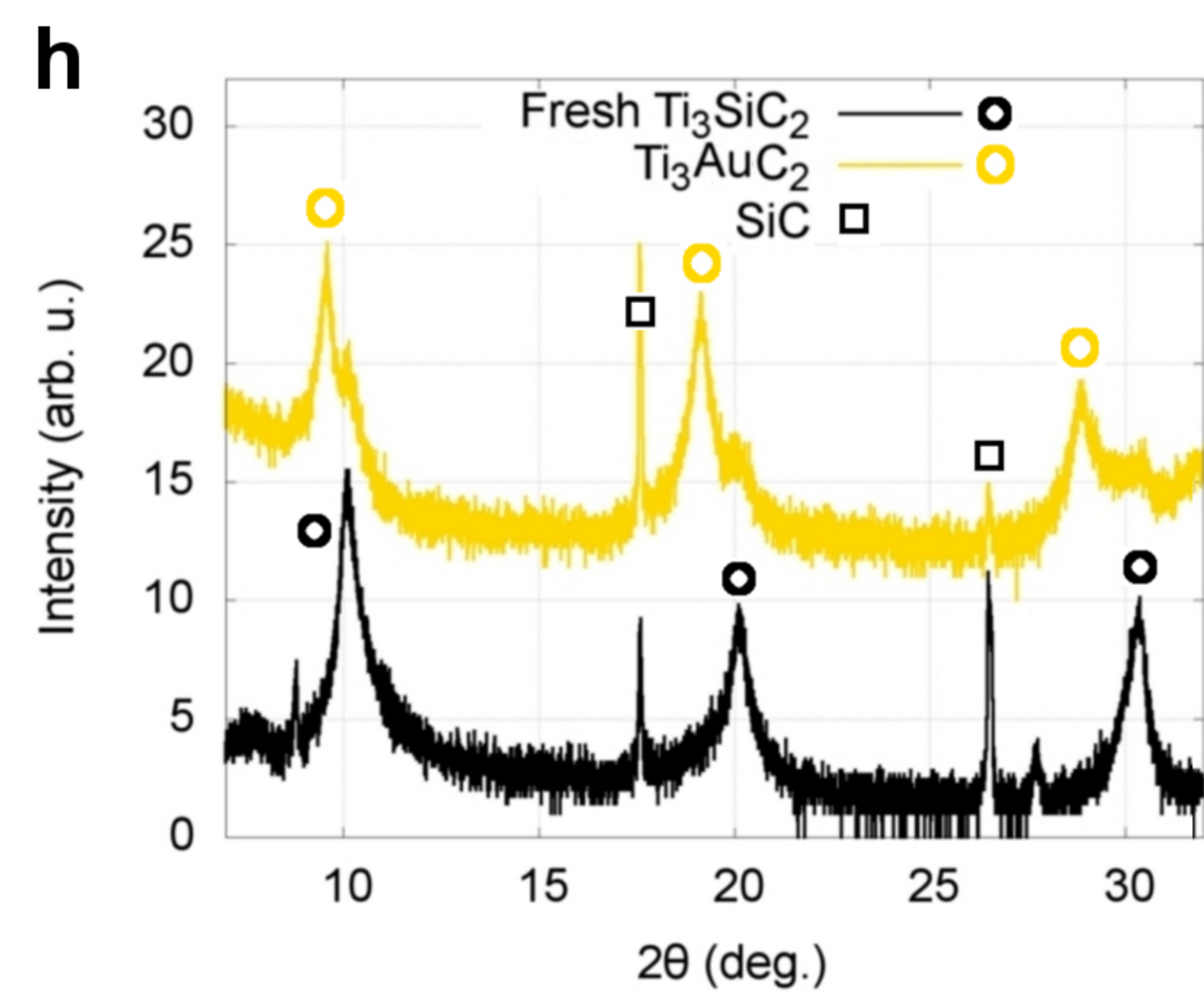
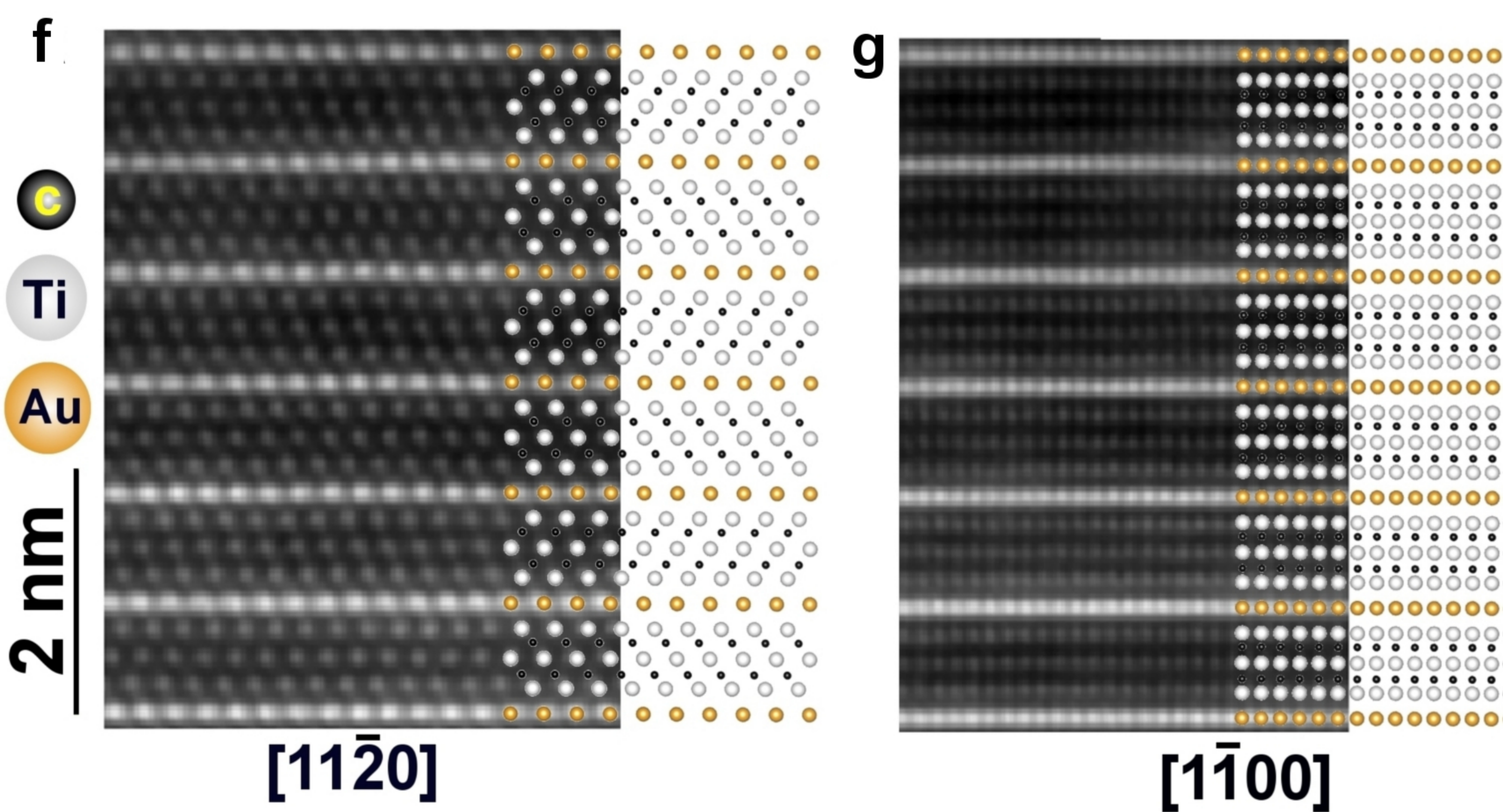
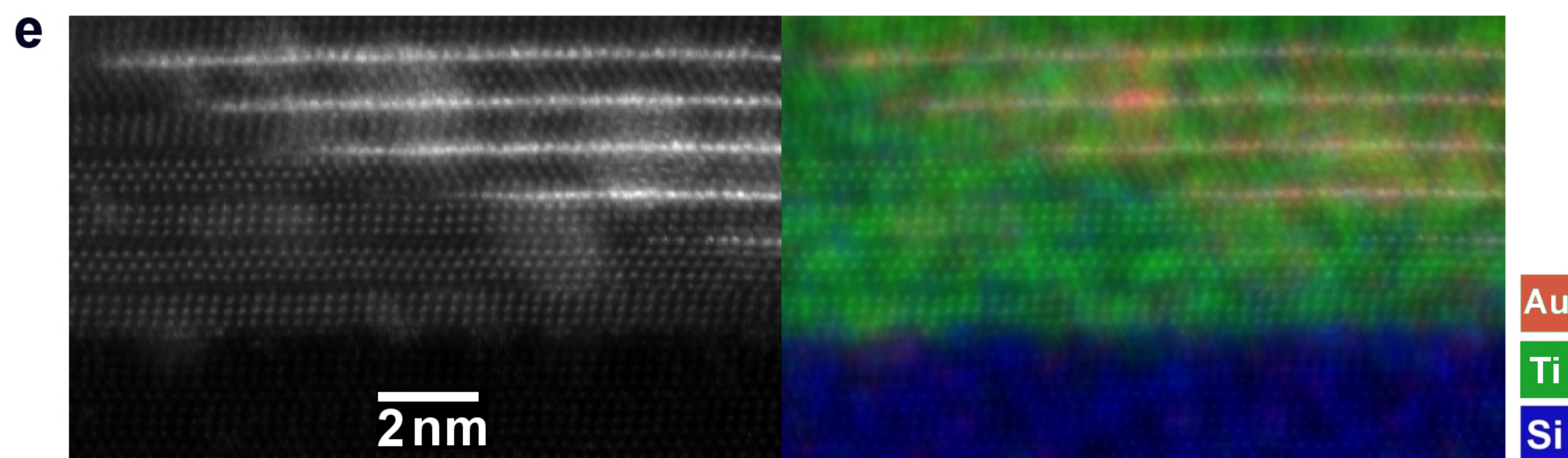
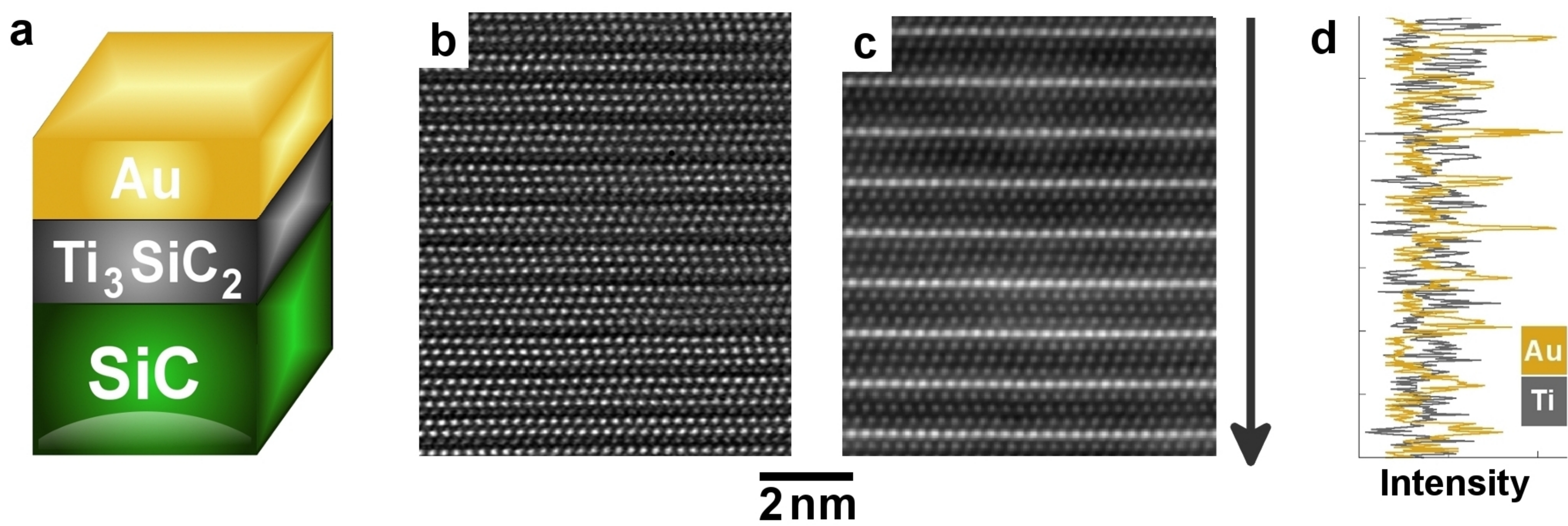
403

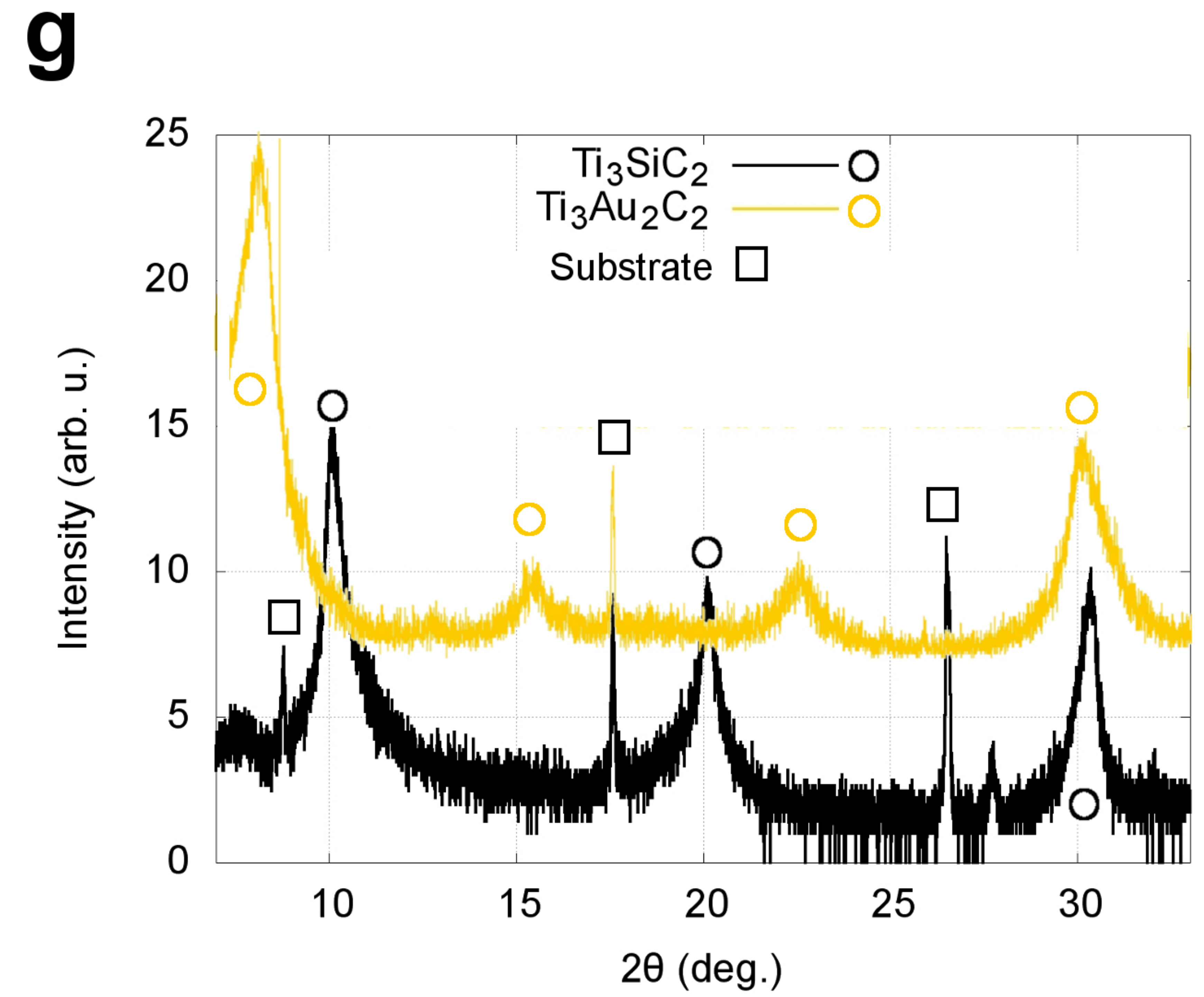
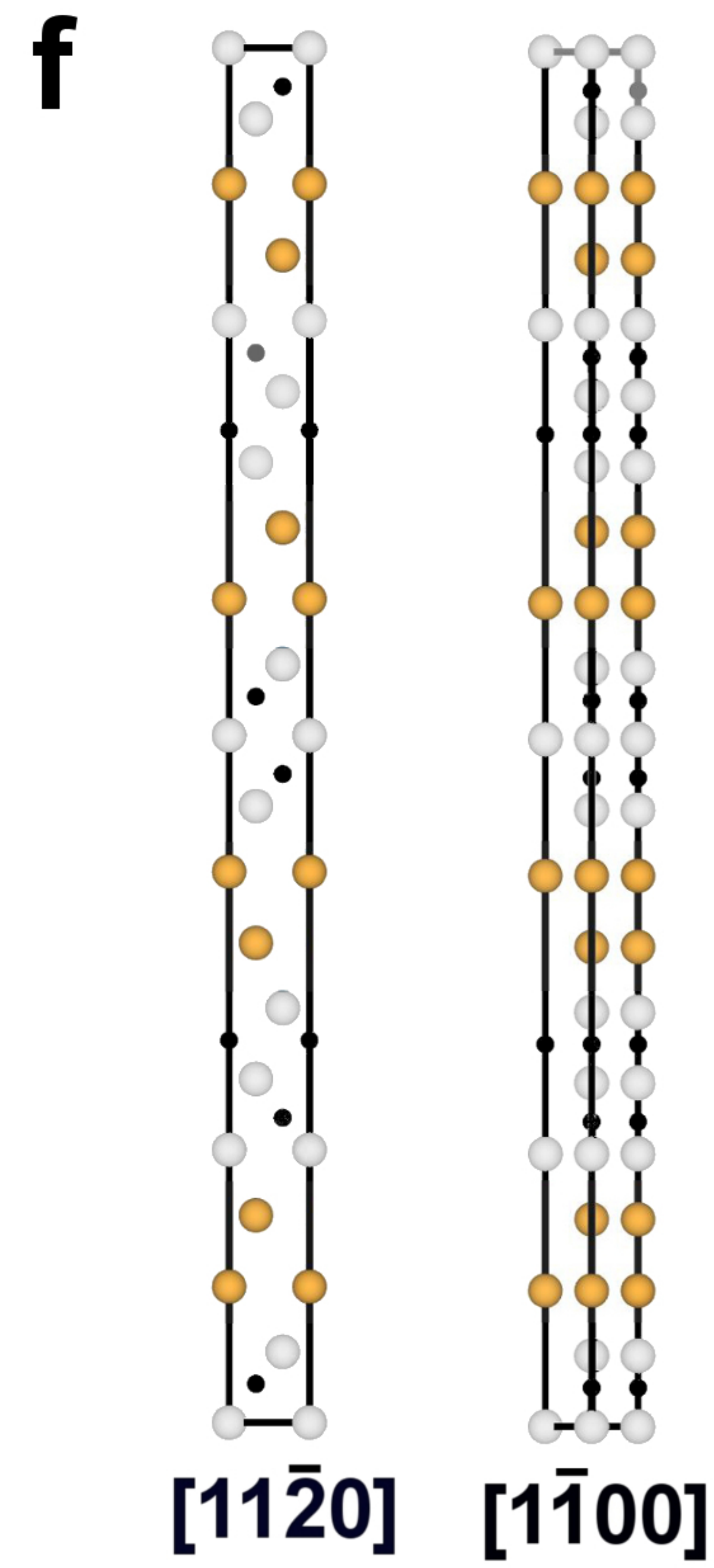
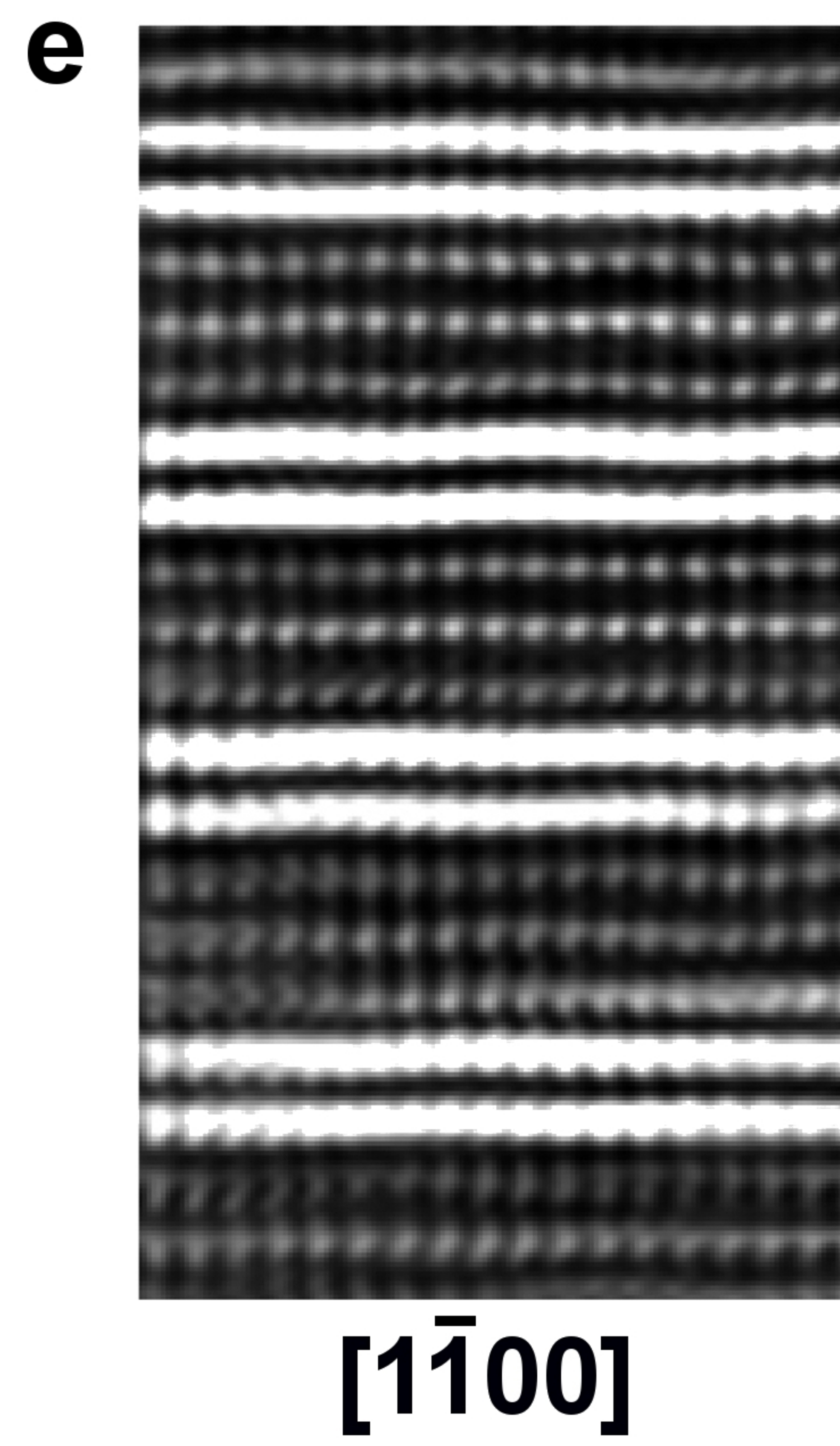
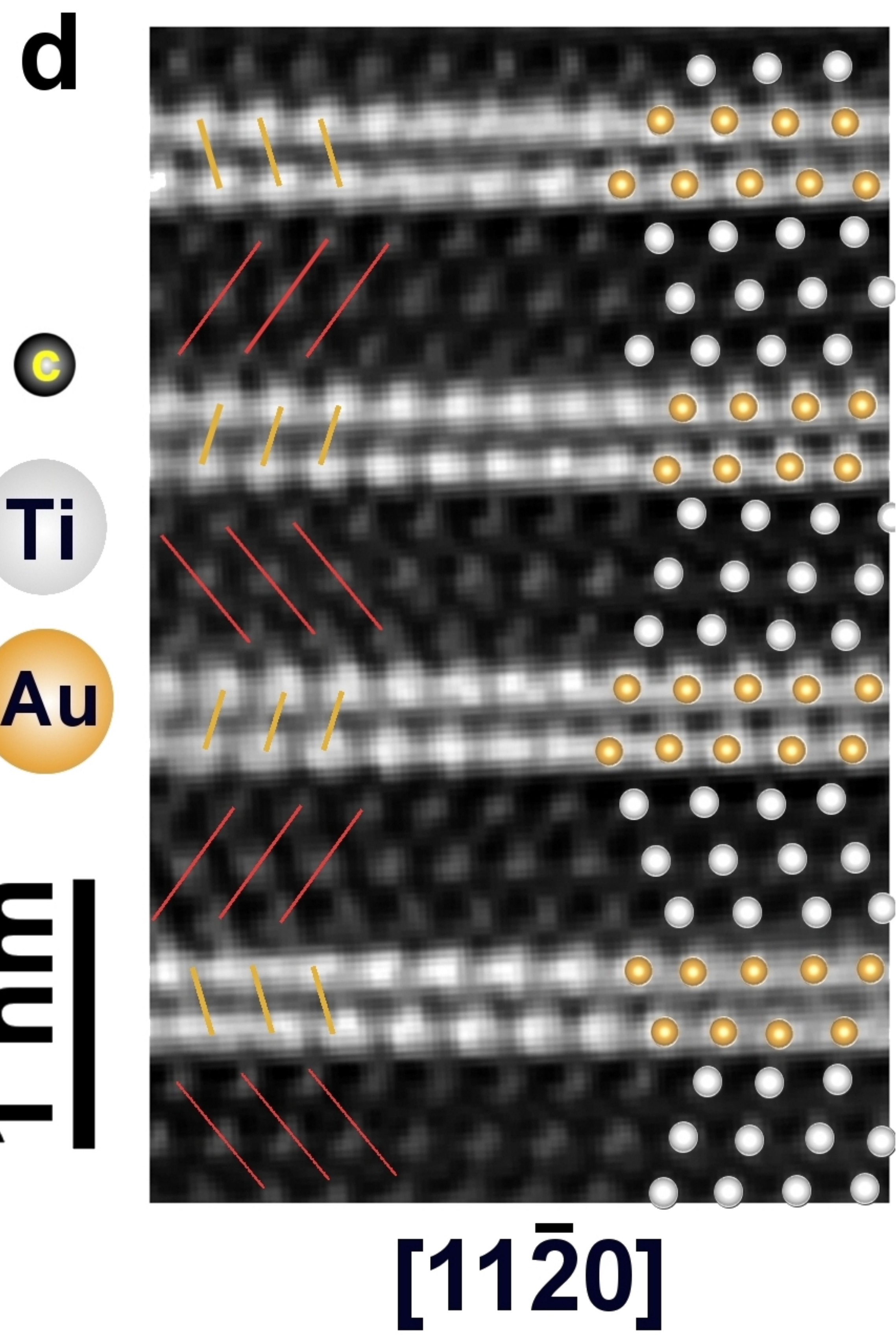
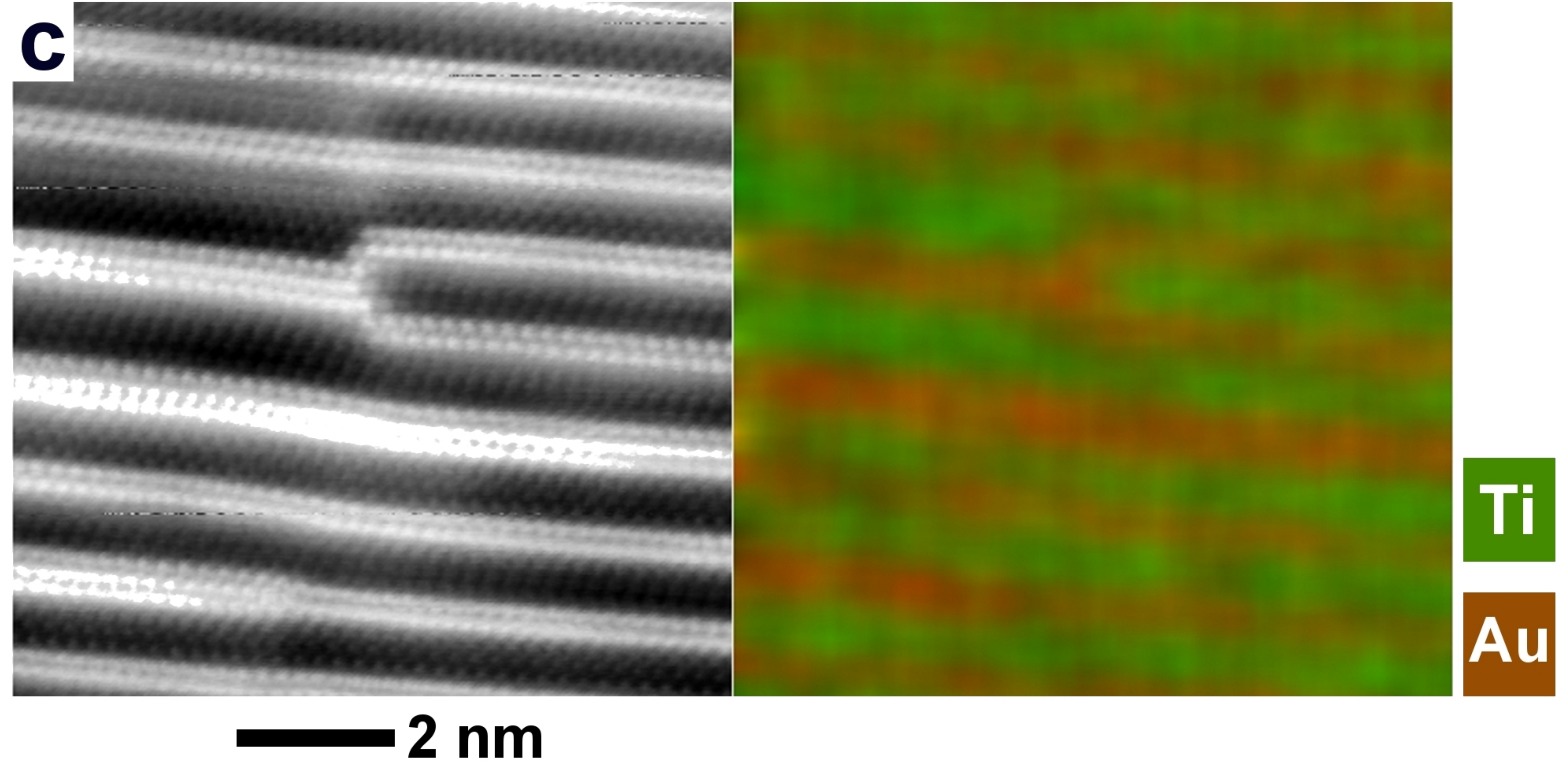
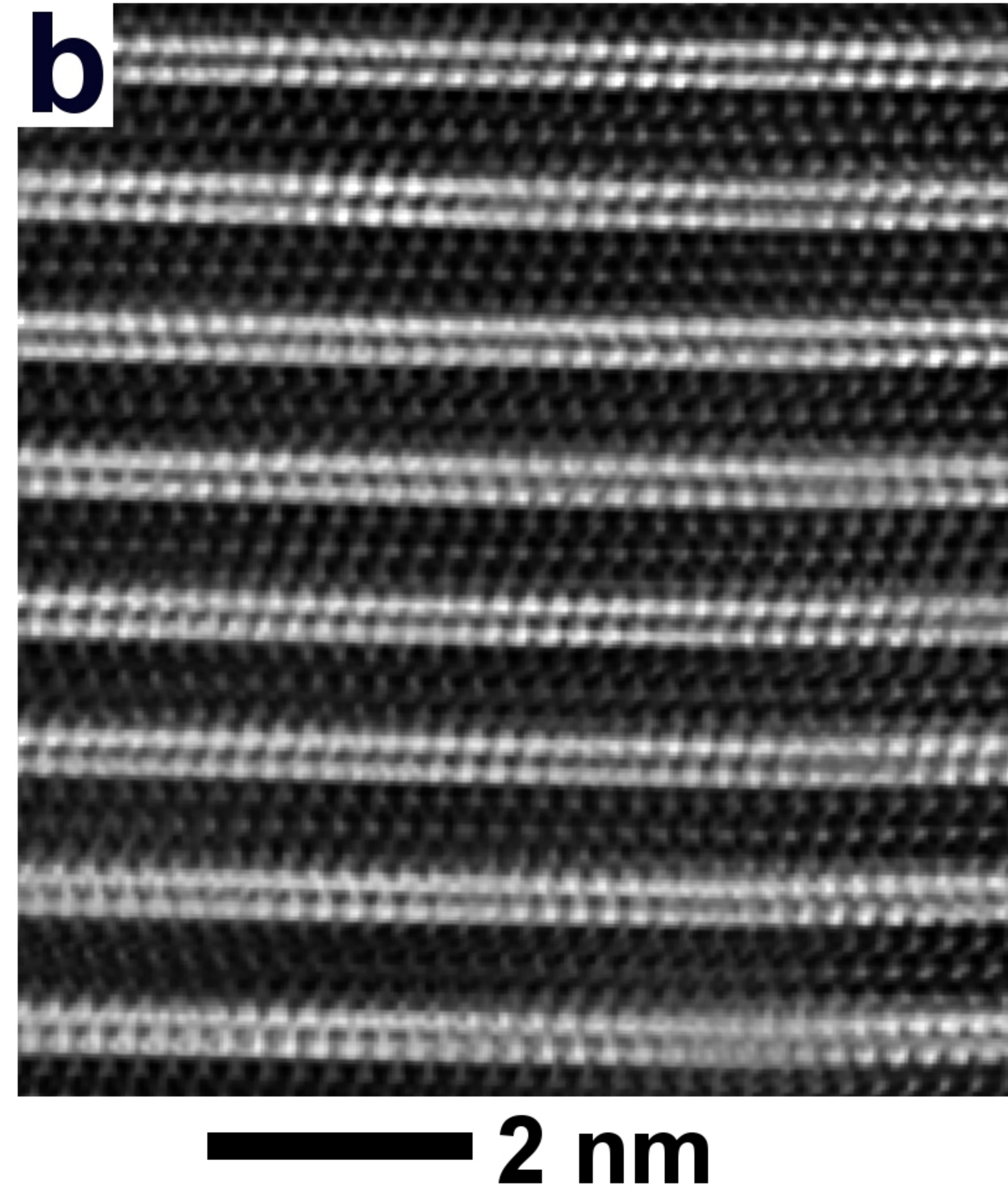
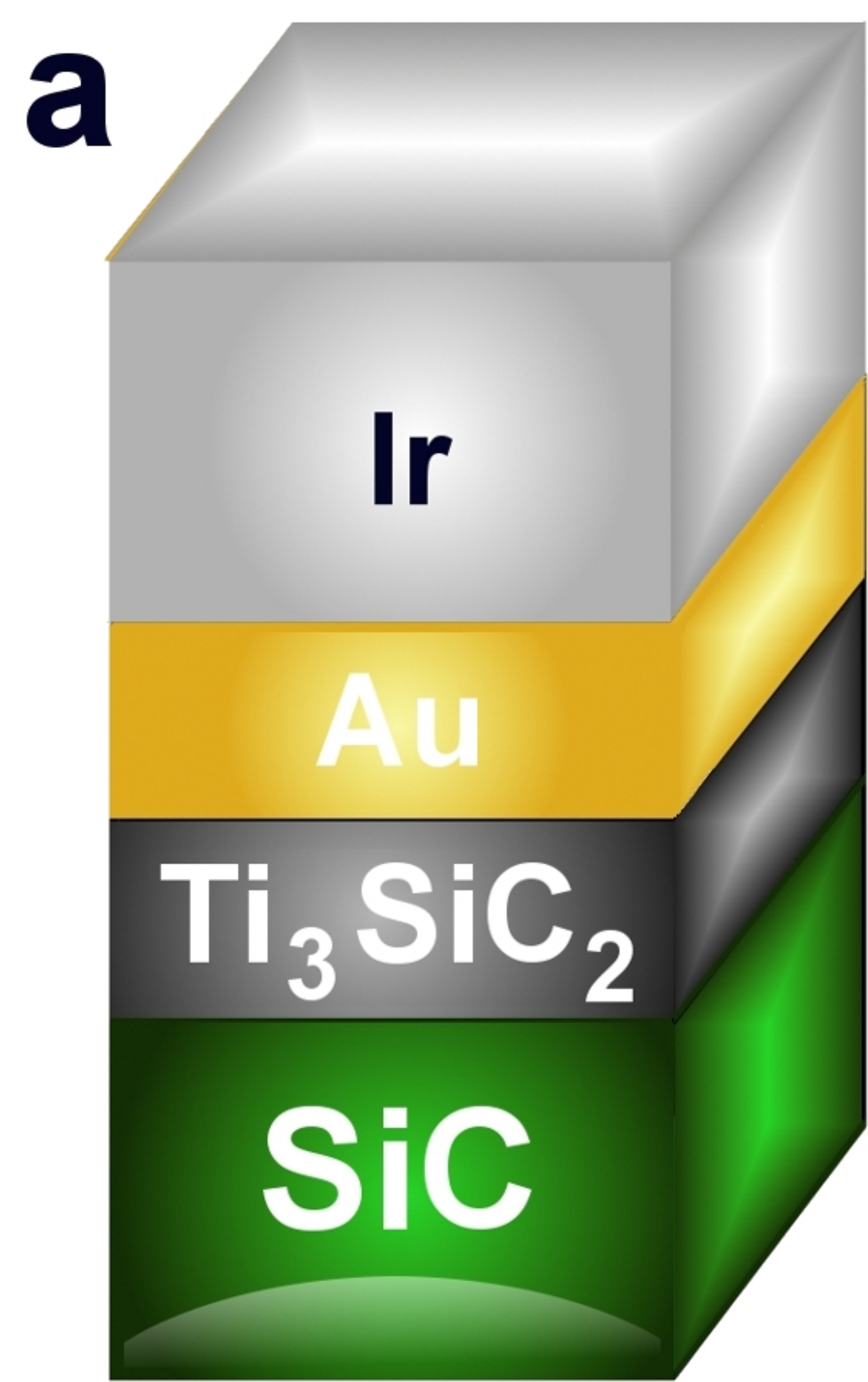
404

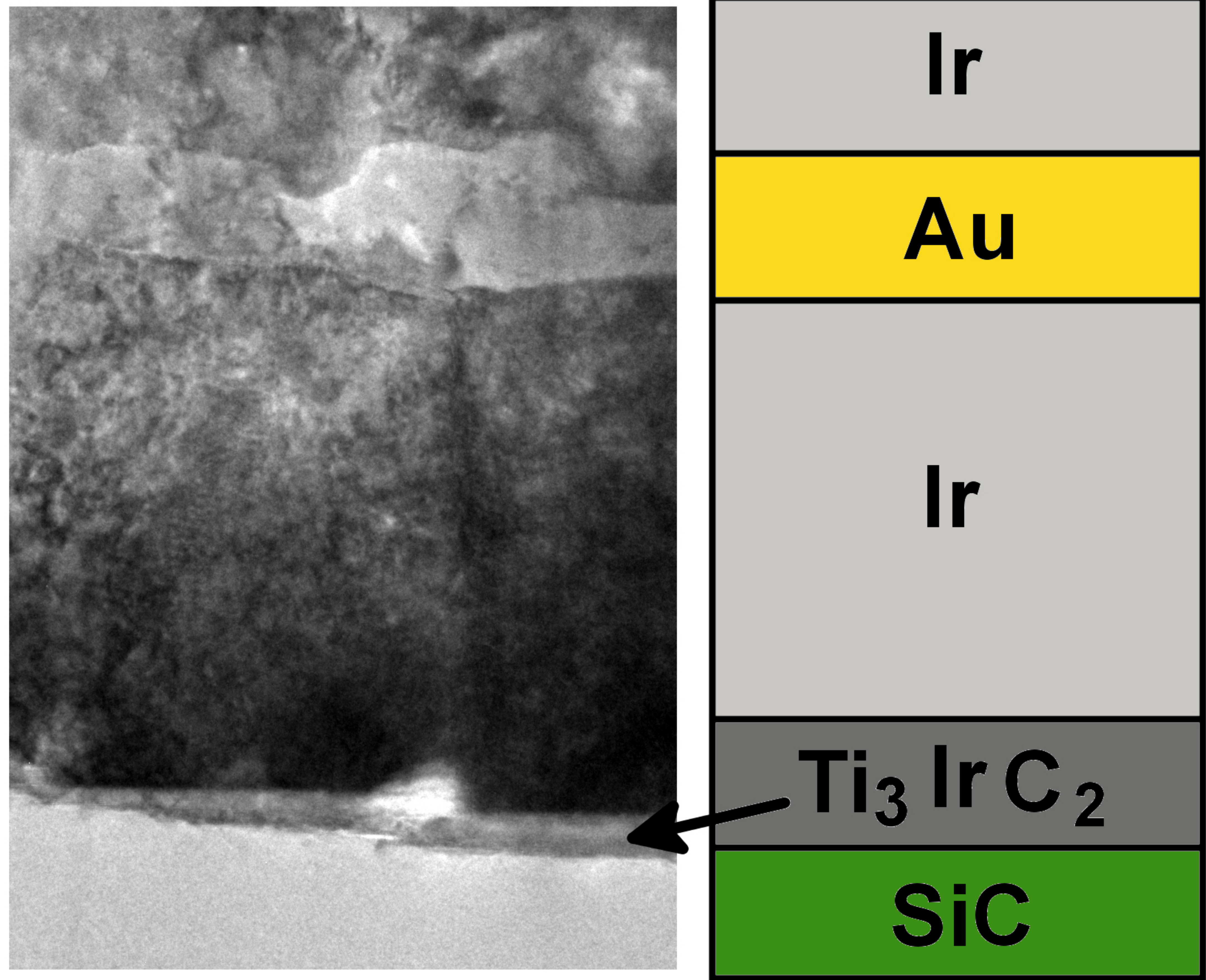
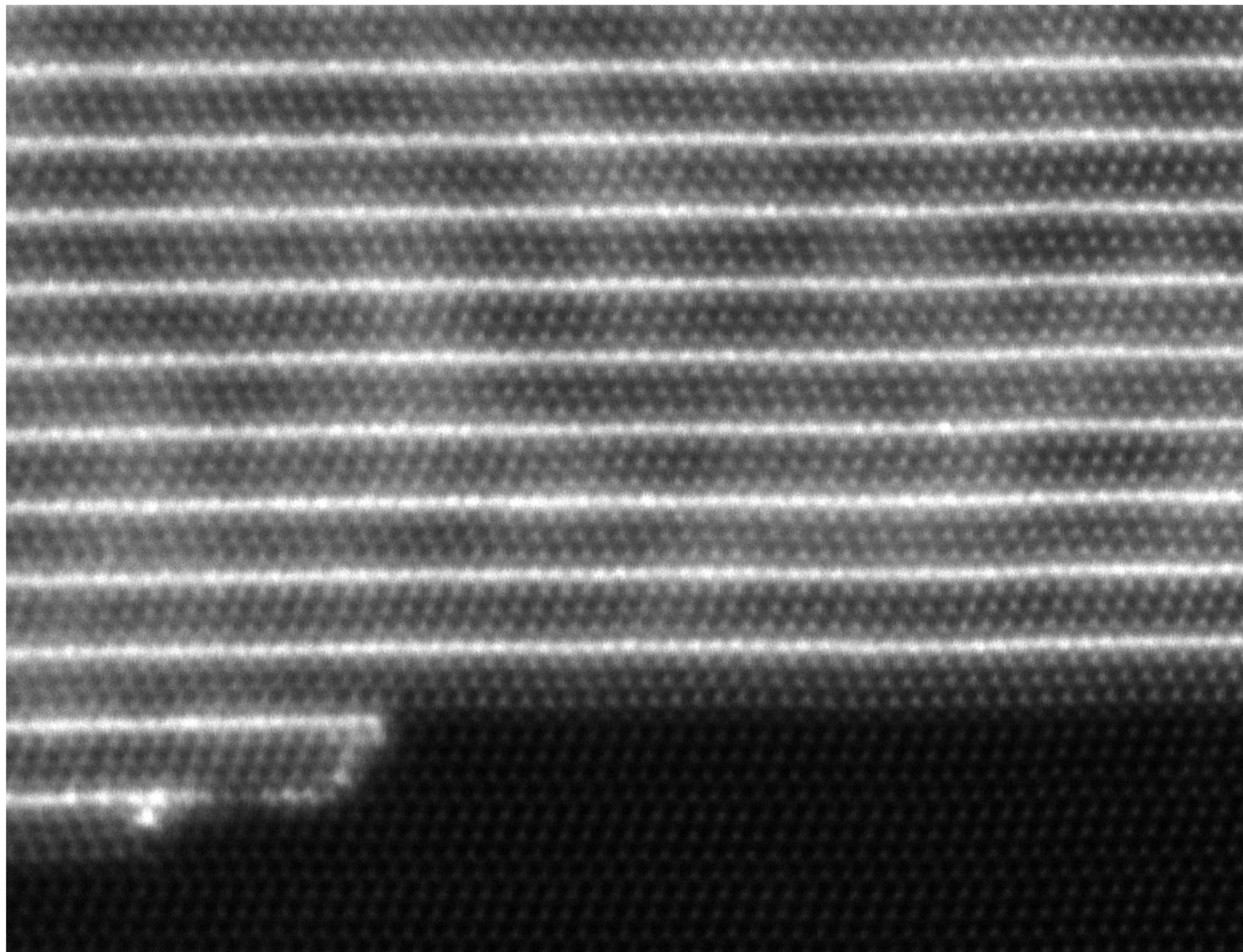
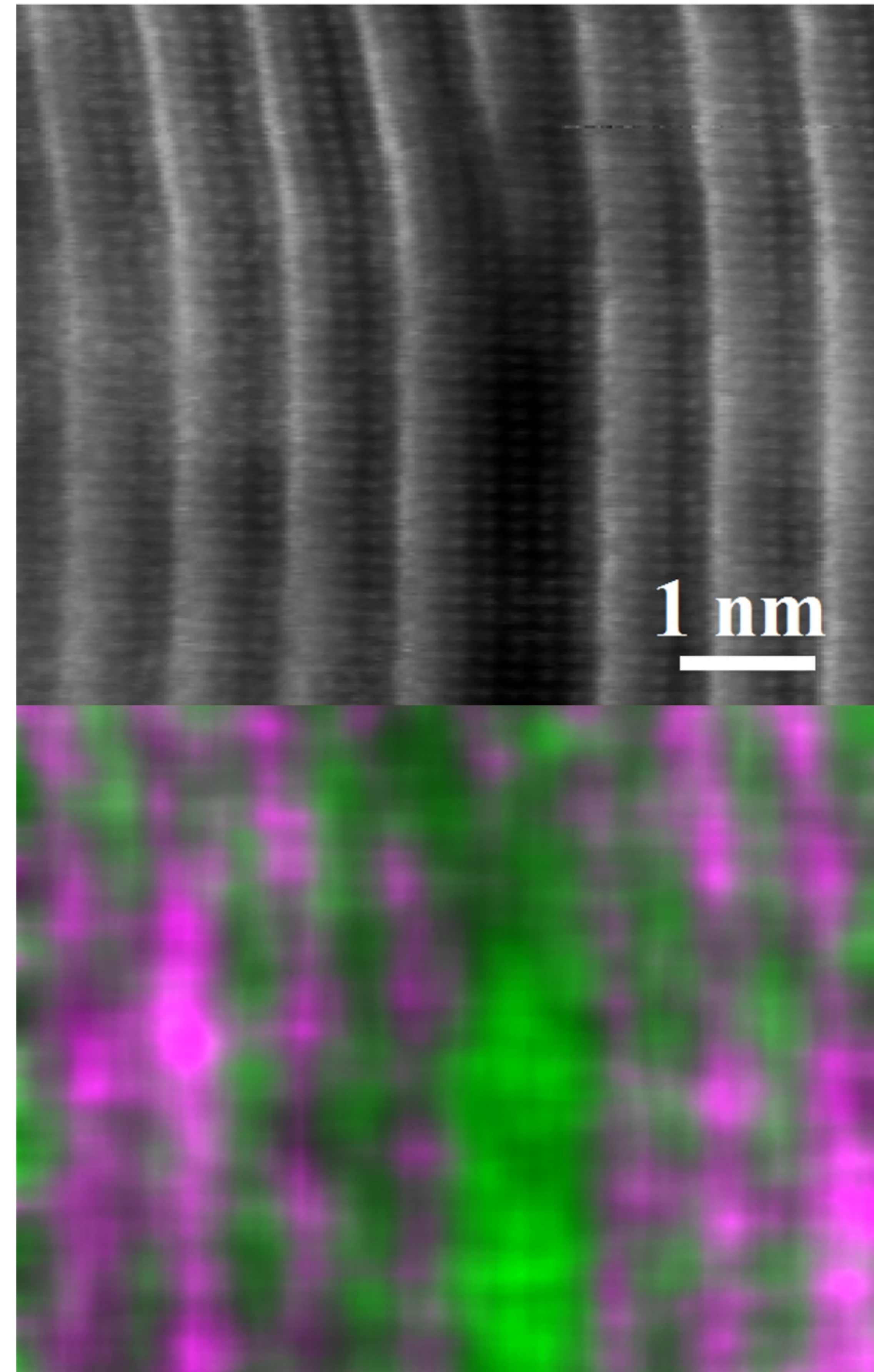


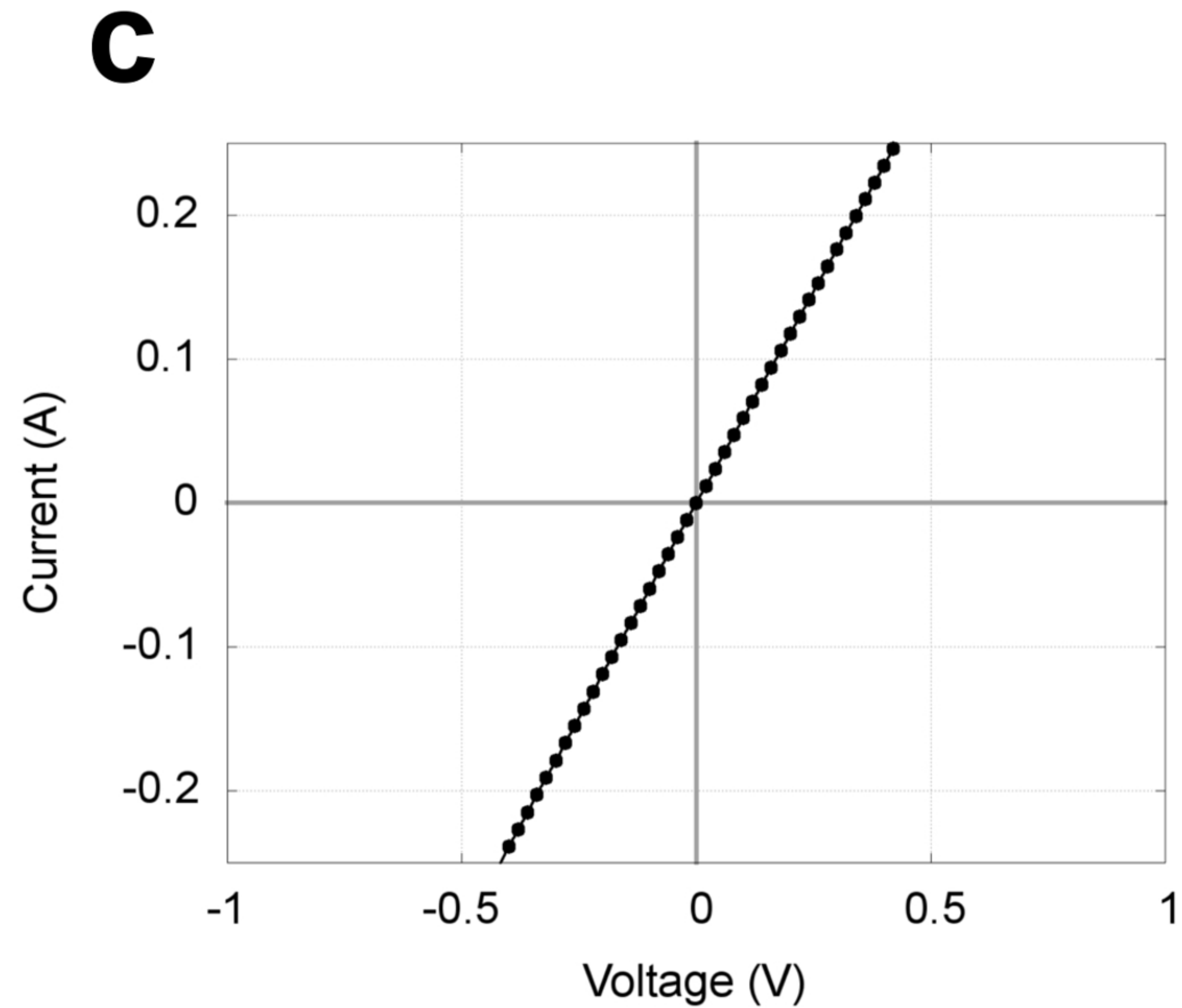
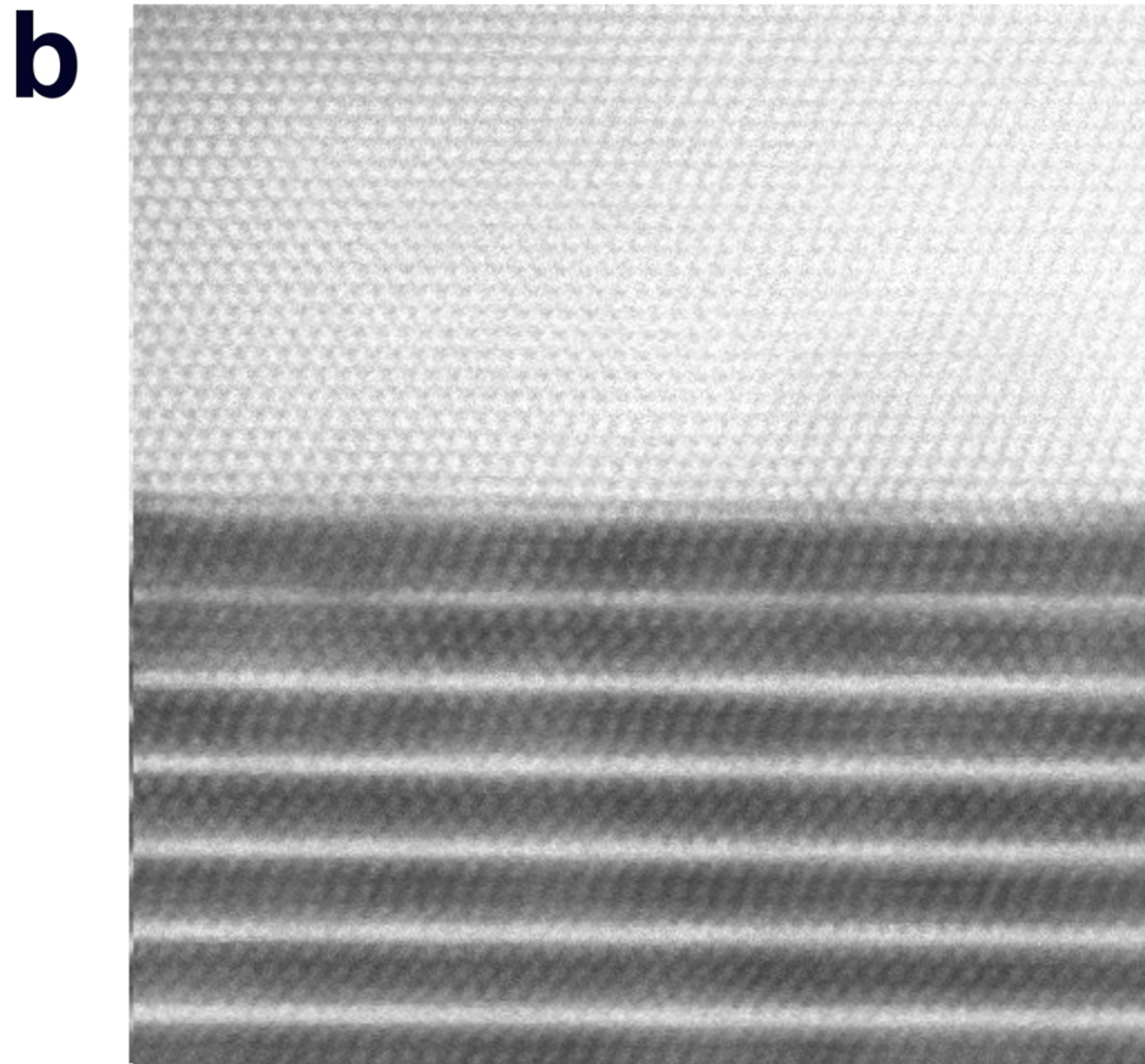
405

406 **Figure 4. Stability of Ti_3AuC_2 based ohmic contact at 600 °C.** (a) Schematic illustration of
 407 the as-deposited ohmic contact structure, (b) and (c) the interface between the Au and the
 408 Ti_3AuC_2 sites and the current/voltage curve after 1000 h of aging at 600 °C, respectively.





a**b****c****Ti****Ir**



Supplementary information for

Synthesis of Ti_3AuC_2 , $\text{Ti}_3\text{Au}_2\text{C}_2$ and Ti_3IrC_2 by noble-metal substitution reaction in Ti_3SiC_2 for high-temperature-stable ohmic contacts to SiC

Hossein Fashandi, Martin Dahlqvist, Jun Lu, Justinas Palisaitis, Sergei I. Simak, Igor A. Abrikosov, Johanna Rosen, Lars Hultman, Mike Andersson*, Anita Lloyd Spetz*, and Per Eklund*

Department of Physics, Chemistry, and Biology (IFM), Linköping University, SE-581 83 Linköping, Sweden

KEYWORDS: Layered phases, noble metals, MAX phase ohmic contacts, oxidation resistance

Section S1. Si out-diffusion

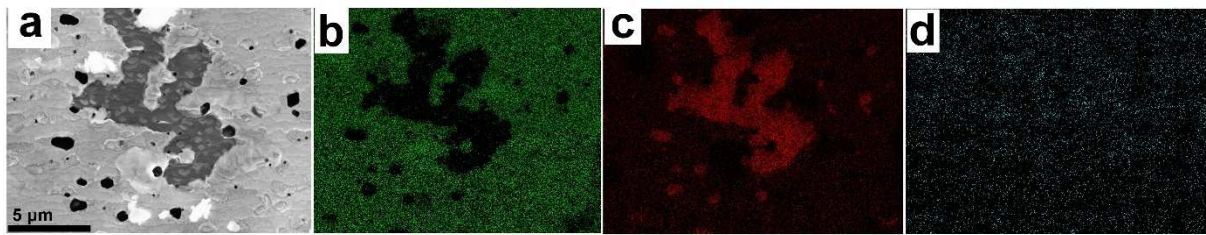


Figure S1. Scanning electron microscopy (SEM) images of the surface of annealed SiC/Ti₃SiC₂/Au. (a) SEM image showing different islands formed on the surface after annealing, (b) Energy dispersive X-ray spectroscopy of Au M α signal showing the dark islands to be deficient in Au, (c) that of Si K α showing the dark islands to be Si-rich, (d) that of Ti K α which rules out any of the dark regions to be exposed Ti₃SiC₂ or Ti₃AuC₂.

Section S2. Computational details

First-principles calculations were performed by means of density functional theory (DFT) and the projector augmented wave method^{1,2} as implemented within the Vienna *ab-initio* simulation package (VASP)³⁻⁵. We adopted the generalized gradient approximation (GGA) as parameterized by Perdew-Burke-Ernzerhof (PBE)⁶ for treating electron exchange and correlation effects. Calculations including spin-orbit coupling have been performed in the mode implemented in VASP by Hobbs et al.⁷ and Marsman and Hafner⁸ and performed in two steps. First a scalar-relativistic calculation has been performed to obtain the correct geometry. In those cases where the ternary phase contains Au or Ir we used the ground state resulting from the scalar-relativistic calculations to initialize the calculations including spin-orbit coupling. A plane-wave energy cut-off of 500 eV was used and for sampling of the Brillouin zone we used the Monkhorst-Pack scheme⁹. For each considered phase, the geometric and electronic degrees of freedom were relaxed simultaneously until the change in total energy between successive iteration steps was smaller than 10^{-6} eV. Calculations were performed at zero temperature and pressure and all structures were fully relaxed.

Thermodynamic stability at 0 K is expressed as formation enthalpy ΔH_{cp} and calculated by comparing its total energy with respect to competing phases. Included competing phases are based on experimental phase diagrams and what is present in similar systems (see section S6). In order to find which combination of competing phases having the lowest energy we apply a linear optimization procedure based on the simplex method. Further details are given in Refs.^{10,11} To determine the dynamical stability of the studied ordered structure, we performed phonon calculations using the small displacement method, supercell sizes of at least $3 \times 3 \times 1$ unit cells, along with the code Phonopy¹². Density of states (DOS) and chemical bonding were investigated in terms of projected crystal orbital Hamiltonian populations (pCOHP) which were derived using the LOBSTER program^{9,12,13}. Using this method the calculated band-structure energy is reconstructed into orbital interactions. Positive pCOHP values indicate an antibonding interaction, and negative pCOHP values indicate a bonding interaction.

Section S3. Ti-Au-C system

Calculated formation enthalpies ΔH_{cp} along with lattice parameters are shown in Table S1 for $Ti_{n+1}AuC_n$, where $n = 1, 2, 3$. For $n = 1$, ΔH_{cp} is positive indicating that the structure is not stable with respect to its competing phases. However, $n = 2$ and 3 are found stable as seen by their negative ΔH_{cp} . Note that for Ti_3AuC_2 this is -14 meV/atom. From experiment it was also observed that Au can form a double layer between $Ti_{n+1}C_n$ sheets when replacing Si. Such double A-layer formation has previously been reported for Mo_2Ga_2C with Ga atoms stacked on top of each other. For $Ti_3Au_2C_2$, see Fig. S2(a), such stacking gives a positive ΔH_{cp} , i.e., it is not stable, and it is not observed in TEM where Au atoms are instead in a close-packed arrangement along the [0001]. Based on this information several different candidate stackings were considered. Fig S2(b to d) displays a subset of those. Structure (b) is found to have the lowest energy and be stable (-23 meV/atom), but it has a zig-zig stacking of the $Ti_{n+1}C_n$ sheets. This structure is therefore unlikely taken into account the formation of $Ti_3Au_2C_2$ from Ti_3SiC_2 where the latter have a zig-zag stacking. From TEM, we observe the zig-zag stacking of $Ti_{n+1}C_n$ sheets and the zig-zig-zag-zag stacking of the Au double layer along the [0001]. This criterion is fulfilled by the structure seen in Fig S2(c), space group $P\bar{3}m1$, and it is also stable with $\Delta H_{cp} = -21$ meV/atom. Further crystallographic information for the $P\bar{3}m1$ structure is given in Table S2.

Table S1. Considered atomic stackings, calculated formation enthalpy and lattice parameters for $Ti_{n+1}AuC_n$, where $n = 1, 2, 3$ and $Ti_3Au_2C_2$. The influence of spin-orbit coupling on ΔH_{cp} have been considered for selected phases; the corresponding values are given within parenthesis.

Phase	Space group	a (Å)	c (Å)	ΔH_{cp} (meV/atom)	Competing phases
Ti_2AuC	$P6_3/mmc$ (#194)	3.0686	13.741	+13	Ti_3AuC_2 , $TiAu$
Ti_3AuC_2	$P6_3/mmc$ (#194)	3.0852	18.633	-14 (-14)	Ti_4AuC_3 , $TiAu$
Ti_4AuC_3	$P6_3/mmc$ (#194)	3.0868	23.578	-1 (-1)	Ti_3AuC_2 , TiC
$Ti_3Au_2C_2$	$P6_3/mmc$ (#194)	3.0852	23.831	+12	TiC , $TiAu_2$
	$P3m1$ (#156)	3.0977	34.393	-23	TiC , $TiAu_2$
	$P\bar{3}m1$ (#164)	3.0972	45.876	-21 (-11)	TiC , $TiAu_2$
	$R\bar{3}m$ (#166)	3.0972	68.811	-21	TiC , $TiAu_2$

Table S2. Calculated crystallographic information for $Ti_3Au_2C_2$ with space group $P\bar{3}m1$ (#164). Wyckoff positions are given for each unique crystallographic site. Structure illustrated in Fig. S2(c).

Element	Wyckoff symbol	Symmetry	x	y	z
Ti	1a	$\bar{3}m.$	0	0	0
Ti	1b	$\bar{3}m.$	0	0	1/2
Ti	2c	3m.	0	0	0.19845
Ti	2d	3m.	1/3	2/3	-0.05163
Ti	2d	3m.	1/3	2/3	0.25003
Ti	2d	3m.	1/3	2/3	0.44843
Ti	2d	3m.	1/3	2/3	0.69835
Au	2c	3m.	0	0	0.09901
Au	2c	3m.	0	0	0.40081
Au	2d	3m.	1/3	2/3	0.15082
Au	2d	3m.	1/3	2/3	0.34902
C	2c	3m.	0	0	0.27820
C	2d	3m.	1/3	2/3	0.02817
C	2d	3m.	1/3	2/3	0.52817
C	2d	3m.	1/3	2/3	0.77814

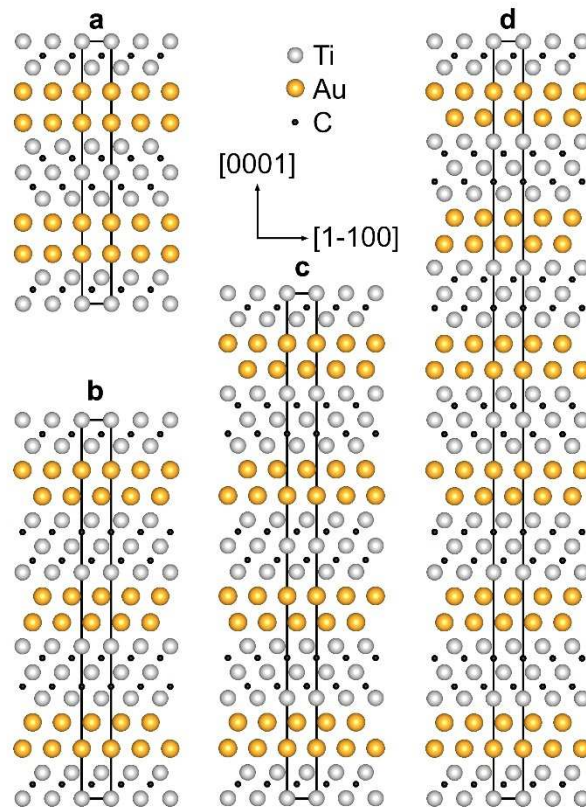


Figure S2. Schematic of $\text{Ti}_3\text{Au}_2\text{C}_2$ crystal structure with different atomic stacking configurations of space group (a) $P6_3/mmc$, (b) $P3m1$, (c) $P\bar{3}m1$, and (d) $R\bar{3}m$.

Section S4. Effect of annealing temperature on the transition from Ti_3SiC_2 to Ti_3AuC_2

Figure S3 shows the XRD patterns for Au/Ti₃SiC₂/Au samples annealed for 12 h at different temperatures. As can be seen, at 600 °C the 0001 peaks of Ti₃SiC₂ coexist with those of Ti₃AuC₂, but the former with considerably higher intensities than the latter. The intensity of the peaks for Ti₃AuC₂ gradually increases with rising the temperature and at 700 °C almost completely dominate those of Ti₃SiC₂.

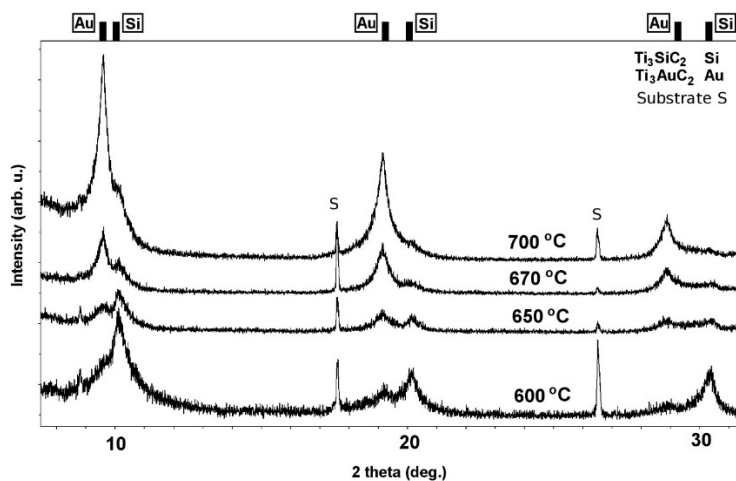


Figure S3. The effect of annealing temperature on the transition from Ti₃SiC₂ to Ti₃AuC₂.

Section S5. Ti-Ir-C system

None of the considered $\text{Ti}_{n+1}\text{IrC}_n$ phases, with $n = 1 - 3$, are found to be stable as seen in Table S3. Instead TiC and TiIr form, the Ti_3IrC_2 phase being metastable. This indicates that the formation of the Ti_3IrC_2 phase is likely supported by kinetic limitations.

Table S3. Calculated formation enthalpy and lattice parameters for $\text{Ti}_{n+1}\text{IrC}_n$, where $n = 1, 2, 3$.

Phase	a (Å)	c (Å)	ΔH_{cp} (meV/atom)	Competing phases
Ti_2IrC	3.0513	12.815	+127	TiC, TiIr
Ti_3IrC_2	3.0452	17.967	+52	TiC, TiIr
Ti_4IrC_3	3.0157	23.523	+42	TiC, TiIr

Section S6. List of competing phases

Table S4. Considered phases with their prototypical structure, calculated equilibrium volume per unit cell, lattice parameters and total energy.

Phase	Prototype structure	Pearson symbol	Space group	V (Å ³ /uc)	a (Å)	b (Å)	c (Å)	E ₀ (eV/f.u.)
Ti	Mg	hP2	P6 ₃ /mmc (194)	34.24	2.924		4.625	-7.762
Ti	Cu	cF4	Fm $\bar{3}$ m (225)	17.10	4.090			-7.706
Ti	W	cI2	Im $\bar{3}$ m (229)	16.95	3.236			-7.662
Si	C (diamond)	cF8	Fd $\bar{3}$ m (227)	40.89	2.734			-5.425
Si		cP46		1070.42	10.229			-5.362
Si		cI16		147.56	6.658			-5.267
Au	Cu	cF4	Fm $\bar{3}$ m (225)	71.83	4.157			-3.220
Ir	Cu	cF4	Fm $\bar{3}$ m (225)	14.52	2.738			-8.848
C	C (graphite)	hP4	P6 ₃ /mmc (194)	38.14	2.464		7.250	-9.225
Ti ₃ Si	Ti ₃ P	tP32	P4 ₂ /n O2 (86)	518.88	10.126		5.060	-30.658
Ti ₅ Si ₃	Mn ₅ Si ₃	hP16	P6 ₃ /mcm (193)	246.59	7.467		5.107	-61.154
Ti ₅ Si ₄	Zr ₅ Si ₄	tP36	P4 ₁ 2 ₁ 2 (92)	547.25	6.703		12.178	-67.508
TiSi	FeB	oP8	Pnma (62)	119.09	6.523	3.643	5.012	-14.704
TiSi ₂	ZrSi ₂	oC12	Cmcm (63)	89.97	3.540	13.562	3.581	-20.289
TiSi ₂	TiSi ₂	oF24	Fddd (70)	84.91	8.258	4.802	8.564	-20.265
Ti ₃ Au	Cr ₃ Si	cP8	Pm $\bar{3}$ n (223)	131.73	5.088			-27.998
Ti ₃ Au	Cu ₃ Au	cP4	Pm $\bar{3}$ m (221)	66.86	4.059			-27.459
TiAu (rt)	CuTi	tP4	P4/nmm O2 (129)	68.07	3.335		6.119	-11.840
TiAu (ht1)	AuCd	oP4	Pmma (51)	67.29	4.686	2.891	4.967	-11.718
TiAu (ht2)	CsCl	cP2	Pm $\bar{3}$ m (221)	34.48	3.255			-11.571
TiAu ₂	MoSi ₂	tI6	I4/mmm (139)	102.53	3.460		8.567	-15.480
TiAu ₄	MoNi ₄	tI10	I4/m (87)	172.95	6.577		3.999	-22.061
Ti ₃ Ir	Cr ₃ Si	cP8	Pm $\bar{3}$ n (223)	124.79	4.997			-34.461
Ti _{1.25} Ir _{0.75}	CsCl	cP2	Pm $\bar{3}$ m (221)	1944.4	3.120			-17.754
TiIr	CsCl	cP2	Pm $\bar{3}$ m (221)	30.21	3.114			-18.112
TiIr	AuCu	tP4	P4/mmm (123)	60.06	4.149		3.490	-18.281
TiIr ₃	Cu ₃ Au	cP4	Pm $\bar{3}$ m (221)	58.07	3.872			-37.138
SiC (6H)	6H-SiC	hP12	P6 ₃ mc (186)	125.97	3.095		15.186	-15.065
β-SiC (3C)	ZnS	cF8	F $\bar{4}$ 3m (216)	84.01	4.380			-15.064
Ti ₂ C	Ca ₃₃ Ge	cF48	Fd $\bar{3}$ m (227)	161.16	8.639			-26.583
TiC _{0.75}	NaCl	cF8	Fm $\bar{3}$ m (225)	81.13	4.329			-15.961
TiC _{0.875}	NaCl	cF8	Fm $\bar{3}$ m (225)	162.7	4.333			-17.263
TiC	NaCl	cF8	Fm $\bar{3}$ m (225)	20.40	4.337			-18.529
TiC	NiAs	hP4	P6 ₃ /mmc (194)	40.83	3.164		4.709	-18.260
(Ti _{0.75} Si _{0.25})C	NaCl	cF8	Fm $\bar{3}$ m (225)	628.6	4.283			-17.032
Ti ₅ Si ₃ C	Mn ₅ Si ₃	hP16	P6 ₃ /mcm (193)	249.40	7.475		5.153	-71.568
Ti ₅ Si ₃ C _{0.5}	Mn ₅ Si ₃	hP16	P6 ₃ /mcm (193)	247.12	7.456		5.133	-66.618
Ti ₅ Si ₃ C _{0.5}	Mn ₅ Si ₃	hP16	P6 ₃ /mcm (193)	494.58	7.454		5.139	-66.623

Ti ₅ Si ₃ C _{0.25}	Mn ₅ Si ₃	hP16	P6 ₃ /mcm (193)	493.56	7.459	5.122	-63.879
Ti ₂ SiC	Cr ₂ AlC	hP8	P6 ₃ /mmc (194)	103.75	3.052	12.861	-33.248
Ti ₃ SiC ₂	Ti ₃ SiC ₂	hP12	P6 ₃ /mmc (194)	145.25	3.076	17.725	-51.916
Ti ₄ SiC ₃	Ti ₄ AlN ₃	hP16	P6 ₃ /mmc (194)	186.26	3.081	22.659	-70.451
Ti ₅ SiC ₄	514-MAX	hP20	P6 ₃ /mmc (194)	227.1	3.080	27.633	-88.956
Ti ₆ SiC ₅	615-MAX	hP24	P6 ₃ /mmc (194)	268.00	3.079	32.642	-107.457
Ti ₅ Si ₂ C ₃	"211+312"	hP20	P6 ₃ /mmc (194)	250.69	3.039	31.339	-84.257
Ti ₅ Si ₂ C ₃	"211+312"	hP30	P3m1 (156)	373.80	3.066	45.904	-85.390
Ti ₅ Si ₂ C ₃	"211+312"	hP30	R $\bar{3}$ m (166)	373.74	3.069	45.814	-85.171
Ti ₇ Si ₂ C ₅	"312+413"	hP42	P3m1 (156)	497.21	3.078	60.583	-122.429
Ti ₂ AuC	Cr ₂ AlC	hP8	P6 ₃ /mmc (194)	112.07	3.069	13.742	-30.451
Ti ₃ AuC ₂	Ti ₃ SiC ₂	hP12	P6 ₃ /mmc (194)	153.61	3.085	18.638	-49.172
Ti ₄ AuC ₃	Ti ₄ AlN ₃	hP16	P6 ₃ /mmc (194)	194.65	3.087	23.584	-67.708
Ti ₂ IrC	Cr ₂ AlC	hP8	P6 ₃ /mmc (194)	103.33	3.051	12.815	-36.302
Ti ₃ IrC ₂	Ti ₃ SiC ₂	hP12	P6 ₃ /mmc (194)	144.29	3.045	17.967	-55.028
Ti ₄ IrC ₃	Ti ₄ AlN ₃	hP16	P6 ₃ /mmc (194)	185.27	3.016	23.523	-73.536

Section S7. Phonon dispersion plots

Figure S4 shows phonon dispersion for four different crystal structures of $\text{Ti}_3\text{Au}_2\text{C}_2$ in panel (a – d), Ti_3AuC_2 in panel (e) and Ti_3IrC_2 in panel (f). All structures are found to be dynamically stable with the exception of $\text{Ti}_3\text{Au}_2\text{C}_2$ in space group $P6_3/mmc$ that exhibits imaginary frequencies at and near the Γ and A high-symmetry points. For Ti_3AuC_2 $P6_3/mmc$ and $\text{Ti}_3\text{Au}_2\text{C}_2$ $P\bar{3}m1$ spin-orbit coupling have been included with negligible effect on the phonon dispersion as compared to the case when spin-orbit coupling is not taken into account.

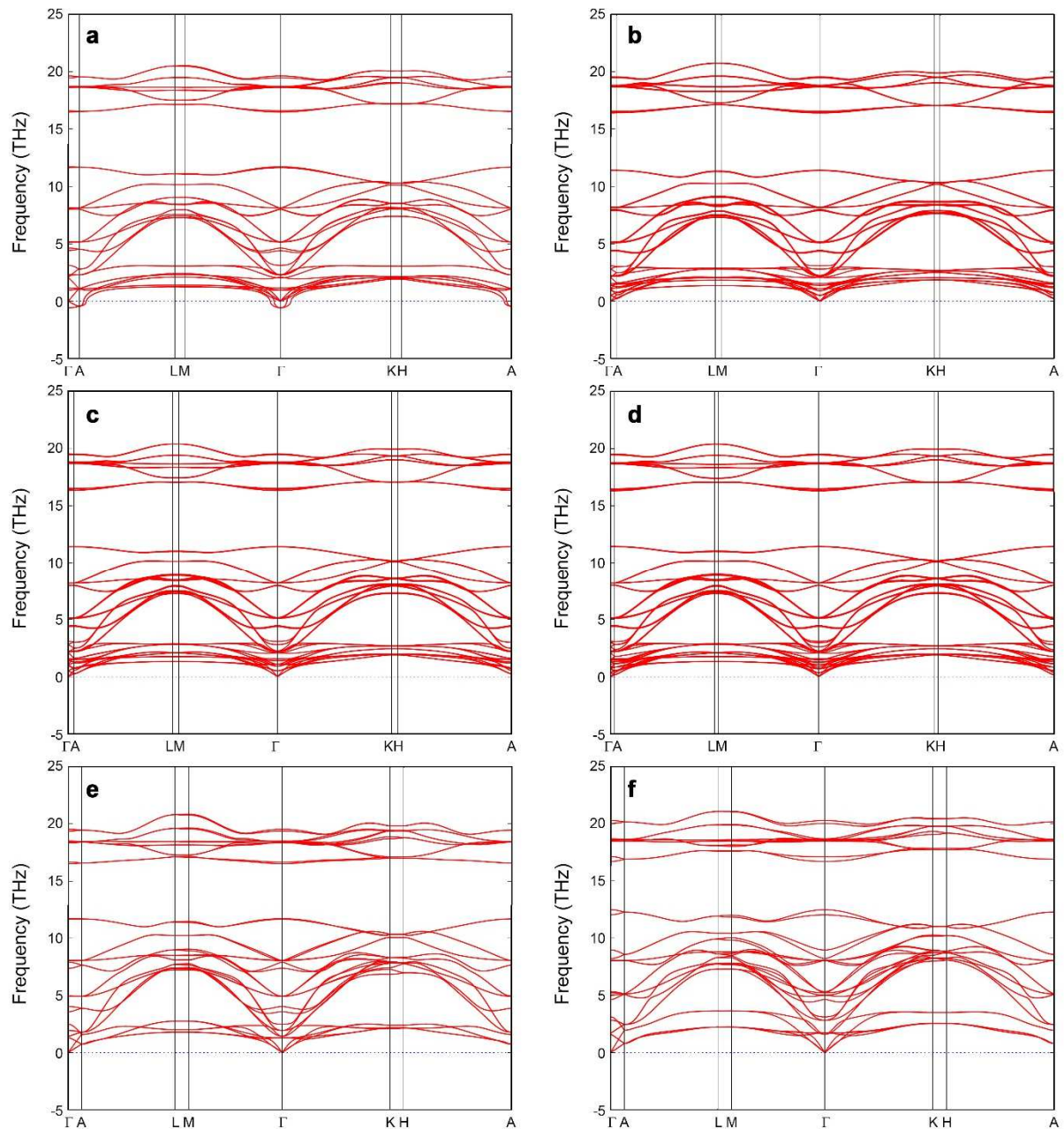


Figure S4. Phonon dispersion for (a) $\text{Ti}_3\text{Au}_2\text{C}_2$ $P6_3/mmc$, (b) $\text{Ti}_3\text{Au}_2\text{C}_2$ $P\bar{3}m1$, (c) $\text{Ti}_3\text{Au}_2\text{C}_2$ $P\bar{3}m1$, (d) $\text{Ti}_3\text{Au}_2\text{C}_2$ $R\bar{3}m$, (e) Ti_3AuC_2 $P6_3/mmc$, and (e) Ti_3IrC_2 $P6_3/mmc$. Schematic representation of $\text{Ti}_3\text{Au}_2\text{C}_2$ structures (a – d) are depicted in Figure S2(a – d). The imaginary frequencies in optical phonon modes for $\text{Ti}_3\text{Au}_2\text{C}_2$ $P6_3/mmc$ in panel (a) can be related to the energetically unfavorable simple hexagonal arrangement of the Au bilayer. This is also reflected by its higher energy as compared to other Au bilayer arrangements, see Table S2.

Section S8. Details on the deposition of IrO_x

We deposited IrO_x on 10×10 mm Al₂O₃ substrates with different partial pressures for Ar and O₂ during the sputtering. The depositions were done at room-temperature. We chose 5, 10, 25, and 50% of O₂ in Ar as the sputtering gas. The resistivity of the corresponding samples were measured using a Jandel four-point probe, as illustrated in Figure S5. As can be seen, the higher oxygen content resulted in the higher resistivity, although, the magnitude of the resistivity still remained low enough, typical of a metallic phase. We chose 25% O₂ for our main experiments regarding formation of oxidation barriers on ohmic contacts to SiC, presented in the main article.

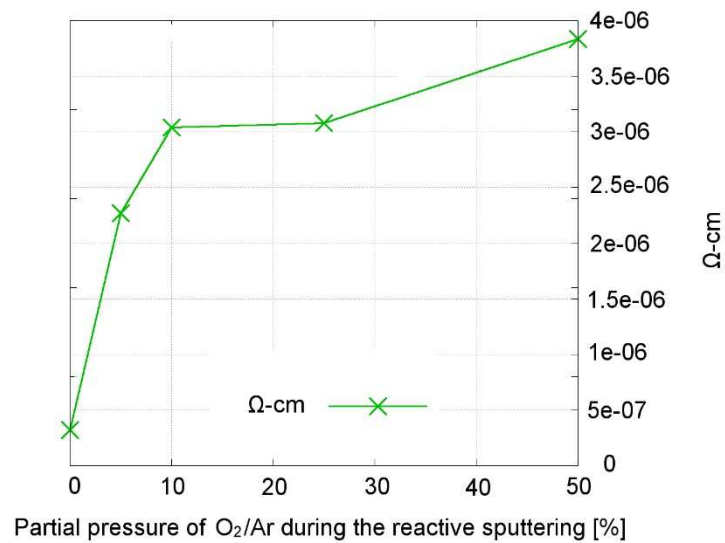


Figure S5. Resistivity of IrO_x films deposited with different oxygen to argon partial pressures.

Section S9. Inter-diffusion between Au and Ir and creation of voids

Figure S.6 shows a low magnification STEM and EDX mapping of a specimen composed of two Ir/Au/Ti₃SiC₂/SiC samples, one fresh (bottom) and one with 12 h of annealing at 600° C (top). This was to ensure that the two experience the same conditions during the TEM sample preparation process. As can be seen, the fresh sample possess sharp borders at the Au/Ir interface, while for the annealed samples interdiffusion and creation of voids is clear. This would result in the structural degradation of the contact.

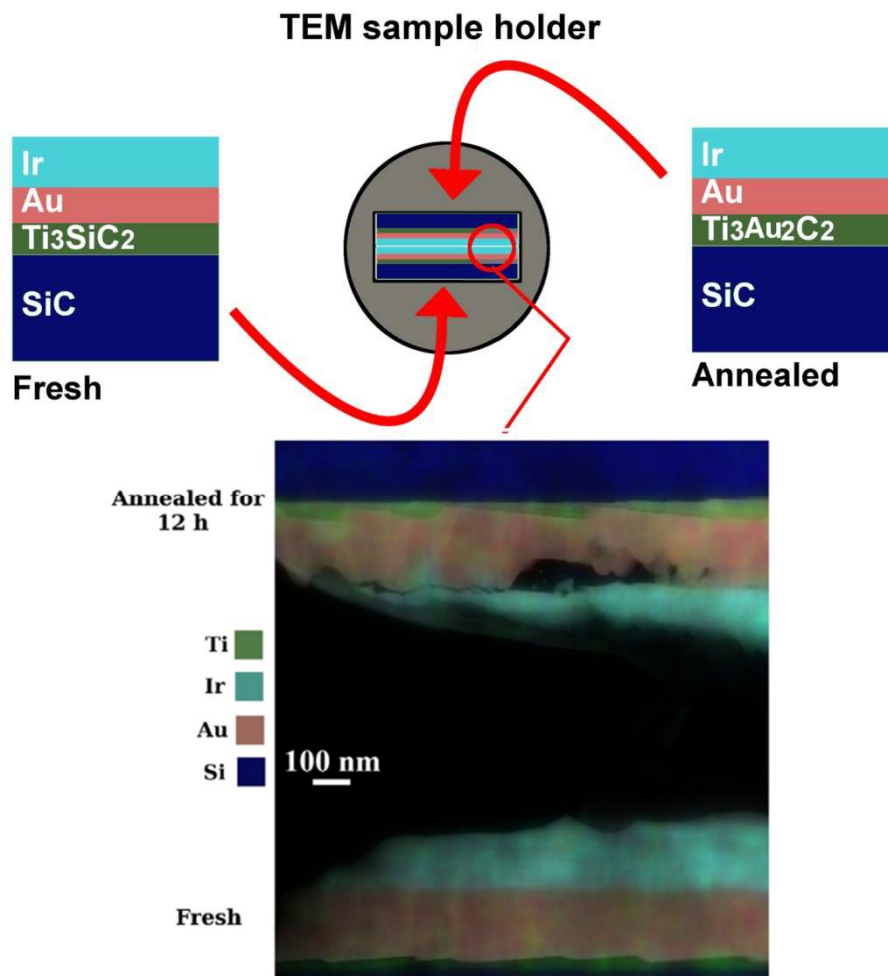


Figure S6. STEM and EDX of two Ir/Au/Ti₃SiC₂/SiC samples inserted into one specimen, one with 12 h of annealing at 600° C (transformed into Ti₃Au₂C₂), and one as-deposited.

Section S10. Degradation of IrO_x/Ti₃SiC₂/SiC ohmic contacts in 600 °C air

We studied the aging of IrO_x/Ti₃SiC₂/SiC ohmic contacts in which the only oxygen barrier was IrO_x deposited directly on Ti₃SiC₂. We kept the sample in 600 °C air for 100 h. Fig. S7 (a) shows the XRD plot of the sample after the aging experiment while Fig.7 (b) demonstrates the I/V curve before and after the aging. As can be seen, the XRD plot shows no signs of 0001 (*l*=2,4, 6) diffraction peaks of Ti₃SiC₂ which appear approximately at 2θ = 10°, 20°, and 30° (see Fig.1 h in the main text). This corresponds to the destruction of the Ti₃SiC₂ phase during the aging process. This is confirmed by the I/V plot. The as-deposited sample shows an ohmic behavior while it acts as an open circuit, *i.e.*, passing no current, after the aging, which corresponds to the complete destruction of the contact area of Ti₃SiC₂/SiC. It should be mentioned that the IrO_x peak appeared at about 28 ° for the annealed sample is due to recrystallization caused during the annealing process at 600 °C. We observed that peak for annealed IrO_x/Al₂O₃ samples as well which rules out its correspondence to any diffraction related to decomposed/oxidized Ti₃SiC₂, *e.g.*, TiO₂.

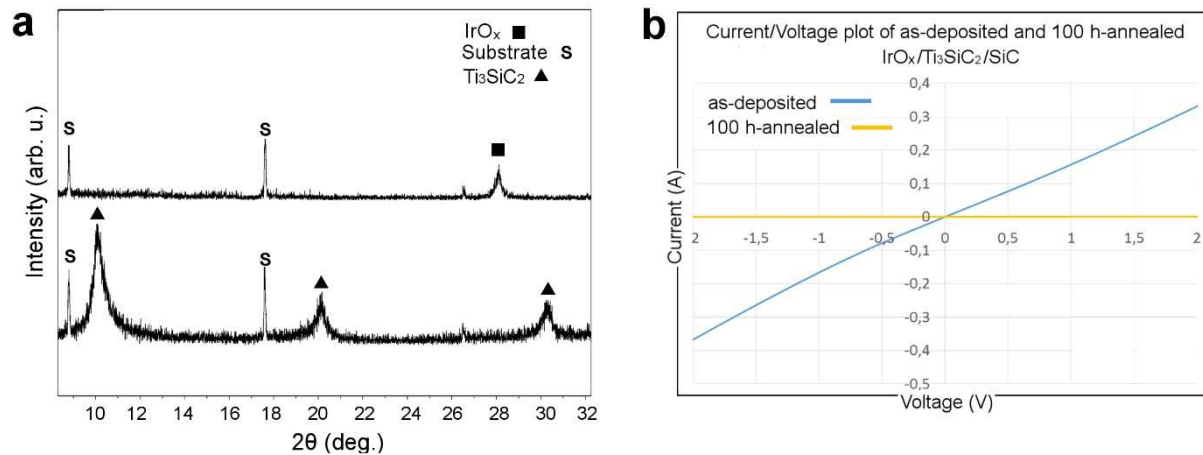


Figure S7. (a) XRD plot after the aging of IrO_x/Ti₃SiC₂/SiC for 100 h at 600 °C air. (b) The I/V curve before and after the aging experiment.

Section S11. Stacking faults in Au-layers.

As discussed in the main text with respect to Fig.2, irregularities in the Au-containing regions can be observed. A possible reason for that can be the presence of stacking faults in the structure of Ti_3SiC_2 host. Fig. S8 shows an overview image of partially formed Ti_3AuC_2 in which two distinct four-layer thick A-layers can be observed. Considering the atomic stacking of the Ti_3C_2 layers, it can be seen that each of those two four-atom thick Au layers are followed by stacking faults in the adjacent Ti_3C_2 layers marked by red a and b signs in the figure.

Fig. S9 is a STEM image from two different crystal orientations of another site Ti_3SiC_2 after the introduction of Au. Similar to Fig. S8, Fig. S9 shows irregularities within Au-containing regions as a result of stacking faults within Ti_3SiC_2 . Au atoms are seen on inclined lattice planes forming ladders between the basal planes of the MAX structure [see Fig S9(a)].

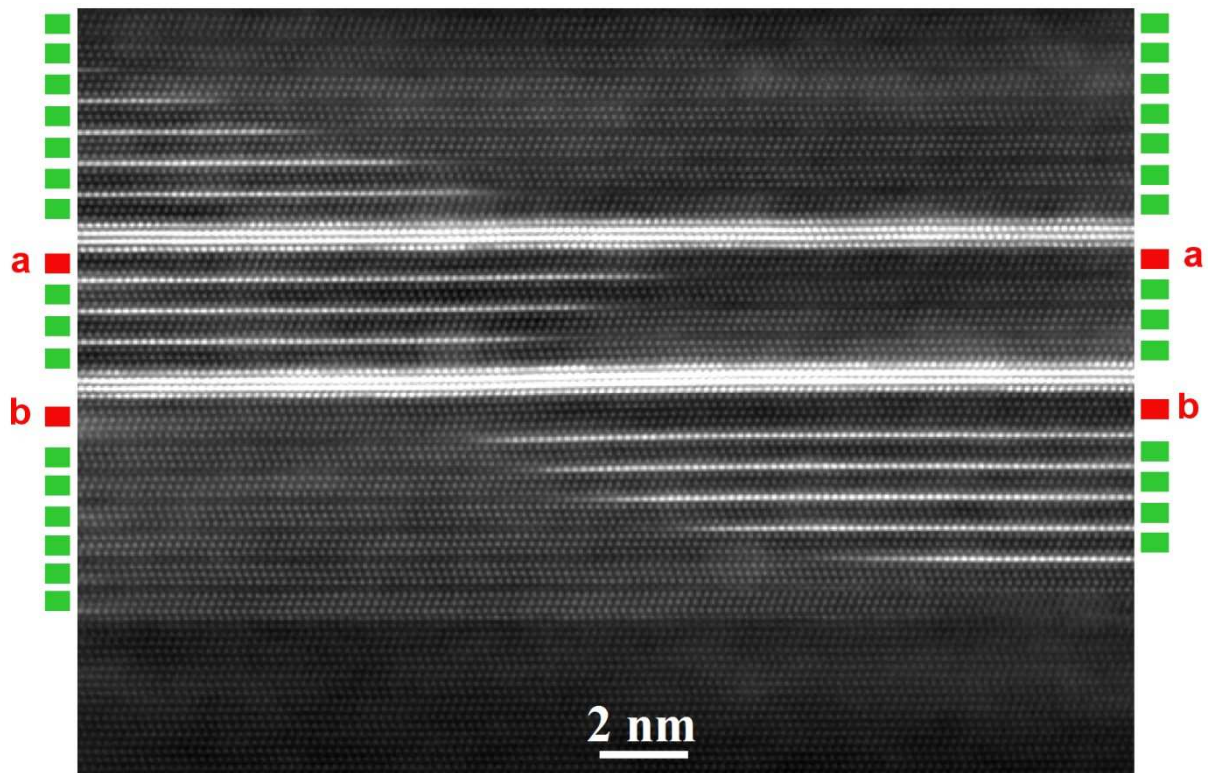


Figure S8. Stacking faults in Ti_3SiC_2 and its influence on the order of the introduction of Au in Ti_3SiC_2 . On the sides of the image, the ordered stackings are marked with green boxes while red boxes refer to stacking faults within the crystal of Ti_3SiC_2 . Red boxes (a) and (b) refer to an inclination fault and the existence of two extra Ti layers (or the absence of a Si layer), respectively.”

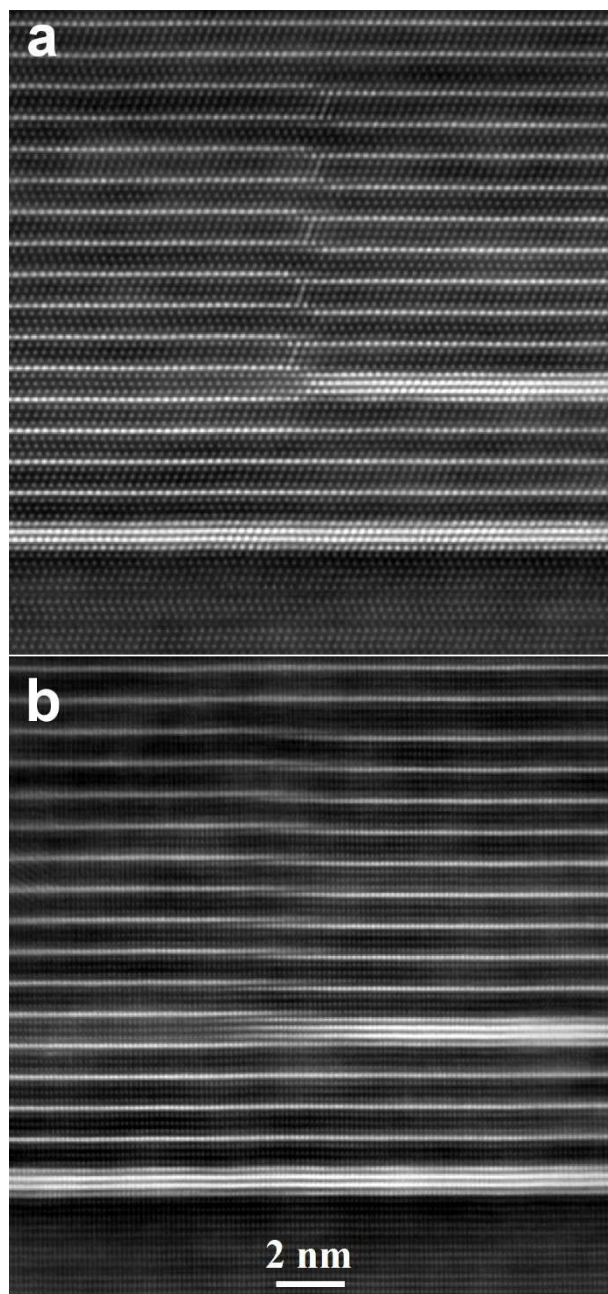


Figure S9. (a) and (b) STEM images of Au-introduction into Ti_3SiC_2 in the same region but viewed through two different directions, $[11\bar{2}0]$ and $[1\bar{1}00]$ for (a) and (b), respectively. Stacking faults for Ti_3C_2 layers has resulted in irregularities for the Au-containing layers.

Section S12. Chemical bonding

We performed electron energy loss spectroscopy (EELS) in order to gain understanding about the chemical bonding of the noble metals in these layered structures. Fig. S10. (a,b, and c) show the EELS spectra of the noble metals in Ti_3AuC_2 , $\text{Ti}_3\text{Au}_2\text{C}_2$, and Ti_3IrC_2 , respectively. Each spectrum is plotted together with that of the corresponding pure noble metal so that any differences between the two with regard to the oxidation states can be revealed. This facilitates identifying the oxidation states of the noble metals.^{14,15} As can be seen, no distinctive shift can be observed between the EELS spectrum of the noble metals in the Ti_3AuC_2 , $\text{Ti}_3\text{Au}_2\text{C}_2$, and Ti_3IrC_2 phases when compared to those of their pure elemental state. In addition, the near-edge fine structure of the peaks are rather identical. These findings indicate a zero (or near-zero) valence state for the noble metals whose bonding state are seemingly of covalent/metallic nature.

Fig. S11. illustrates total and partial electronic density of states (DOS) and projected crystal orbital Hamiltonian populations (pCOHP) of Ti_3SiC_2 as well as those of Ti_3AuC_2 , $\text{Ti}_3\text{Au}_2\text{C}_2$, and Ti_3IrC_2 . DOS and pCOHP of Ti_3SiC_2 (Fig.S.11 (a)), show clear bonding of Ti-C and Ti-Si. Replacing Si with Au in Ti_3AuC_2 (Fig.S.11 (b)), the Au states are shifted down in energy as compared to Si. The Ti-Au do show bonding character but not as strong as Ti-Si in Ti_3SiC_2 as is indicated by smaller integrated pCOHP (IpCOHP) of -1.22 eV/bond for Ti-Au viz. 1.82 eV/bond for Ti-Si. $\text{Ti}_3\text{Au}_2\text{C}_2$ (Fig.S.11 (c)) show many similarities with Ti_3AuC_2 with strong Ti-C bonds and weaker Ti-Au bonds. The Au-Au interaction show both bonding and anti-bonding character between -8 and -2 eV. For the case of Ti_3IrC_2 (Fig.S.11 (d)), the corresponding DOS plot shows rather high densities for Ir as well as Ti(4f) atoms at ≈ 2 -5 eV below the Fermi level. The corresponding pCOHP plot reveals the densities to form comparatively strong Ti-Ir bonding states with IpCOHP = 1.88 eV/bond.

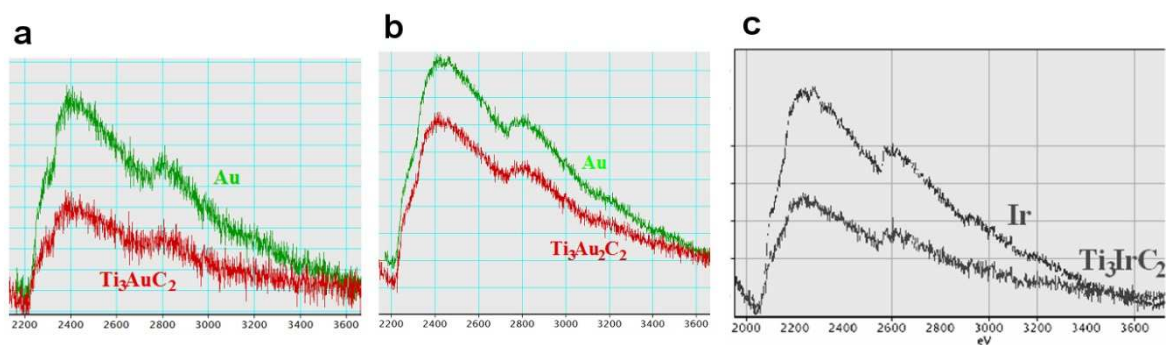


Figure S10. (a,b, and c) the EELS spectra of the noble metals in Ti_3AuC_2 , $\text{Ti}_3\text{Au}_2\text{C}_2$, and Ti_3IrC_2 , respectively, together with that of the corresponding pure noble metal.

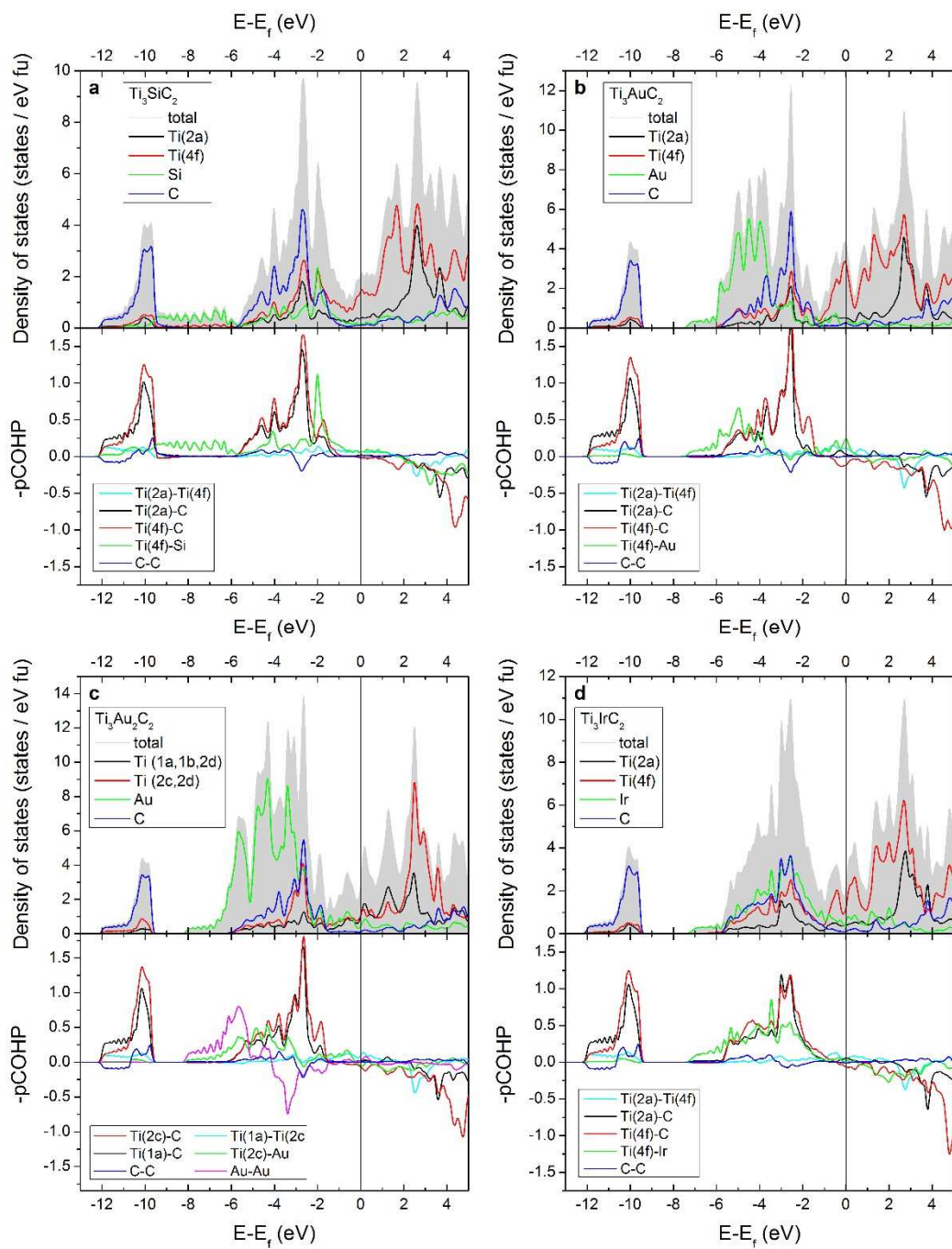


Figure S11. Calculated total and partial density of states DOS (top panel) and projected crystal orbital Hamiltonian populations pCOHP (bottom panel) for (a) Ti_3SiC_2 $P6_3/mmc$, (b) Ti_3AuC_2 $P6_3/mmc$, (c) $\text{Ti}_3\text{Au}_2\text{C}_2$ $P-3m1$, and (d) Ti_3IrC_2 $P6_3/mmc$. Both DOS and pCOHP are obtained using the LOBSTER program.

Section S13. Electronic band structure

In Fig. S12 the electronic band structure is shown for Ti_3SiC_2 , Ti_3AuC_2 , $\text{Ti}_3\text{Au}_2\text{C}_2$ P-3m1, and Ti_3IrC_2 without spin-orbit coupling (black lines) and with spin-orbit coupling (red lines). Including spin-orbit coupling mostly affects bands around -6 to -4 eV below the Fermi level (E_f) where the majority of the Au and Ir states are found but also bands at or close to E_f .

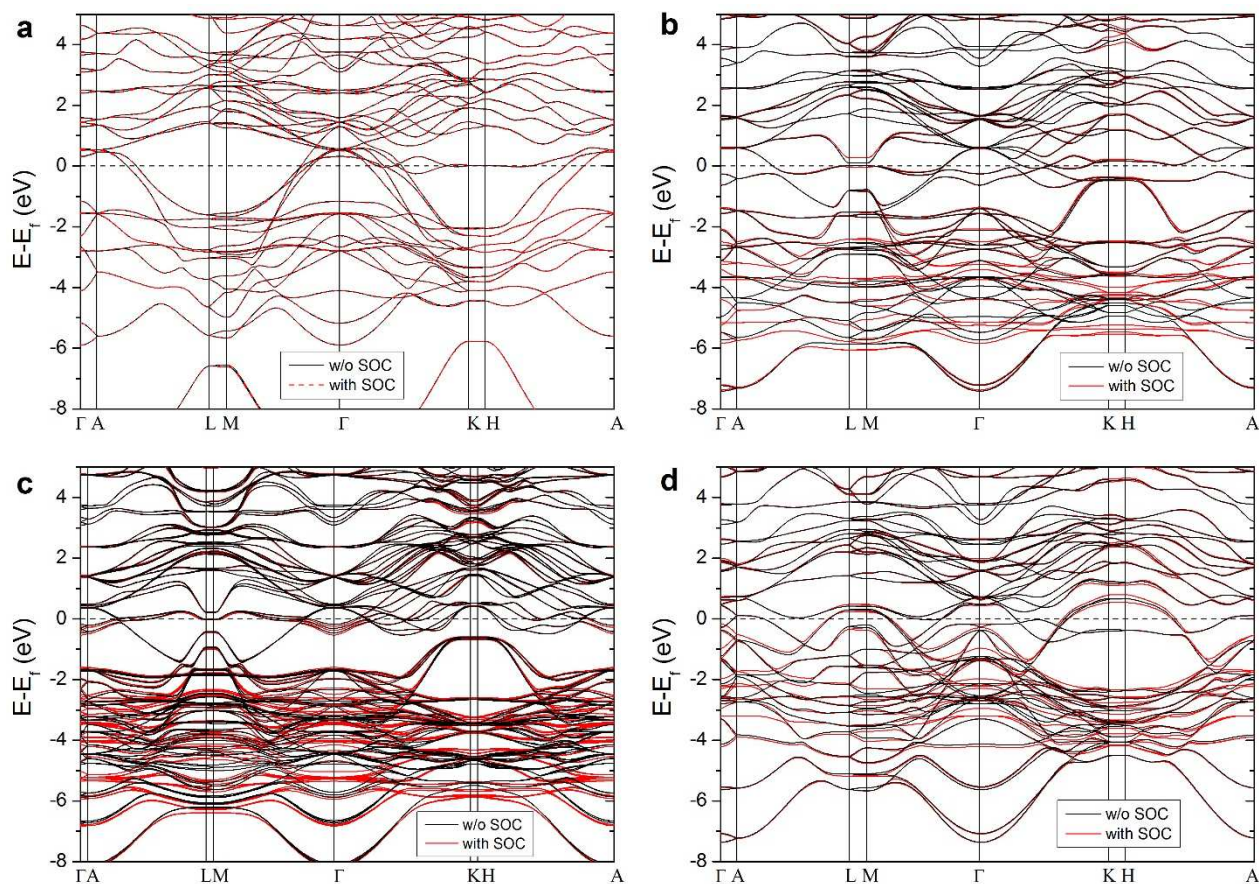


Figure S12. Calculated electronic band structure without spin-orbit coupling (black lines) and with spin-orbit coupling (red lines) for (a) Ti_3SiC_2 P6₃/mmc, (b) Ti_3AuC_2 P6₃/mmc, (c) $\text{Ti}_3\text{Au}_2\text{C}_2$ P-3m1, and (d) Ti_3IrC_2 P6₃/mmc. Au- and Ir-based phases show differences in their electronic band structure when the spin-orbit coupling is considered, see e.g. band splitting at the Fermi level E_f and L-M for Ti_3AuC_2 . For Ti_3SiC_2 , the spin-orbit coupling does not influence the electronic band structure.

Section S14. *In-situ* annealing in TEM

In-situ TEM study details

We applied high-resolution *in-situ* scanning transmission electron microscopy (STEM) to directly visualize the reaction introducing Au into Ti_3SiC_2 during heating. The *in-situ* heating experiments were performed in the double-corrected Linköping FEI Titan³ 60-300 operated at 300 kV, using a MEMS-based double-tilt heating system (DENSsolutions). TEM samples for *in-situ* investigation were prepared from the as-synthesized structure ($\text{Au}/\text{Ti}_3\text{SiC}_2/\text{SiC}$) using the Focused Ion Beam (FIB) lift-out procedure adopted from Duchamp *et al.*¹⁴ The *in-situ* heating started by pre-heating the sample at 400 °C for 10 min, then continuously heating at 450 °C for 4 h. The need for the temperature adjustment with respect to bulk sample heating is because of the TEM geometry where the surface-to-volume ratio is higher. While heating, atomic-resolution STEM high-angle annular dark-field (STEM-HAADF) imaging was carried out using 21.5 mrad convergence angle probe carrying 50 pA current and inner angle of the HAADF detector was set to 40 mrad. STEM-HAADF images were acquired at a frame time of 5 s (image size 1024 px x 1024 px). A series of high-resolution STEM-HAADF images were recorded at representative 3 min time intervals, which were used for constructing the movie.

Movie

The *in-situ* STEM movie (provided as Supplementary video) reveals changes in the STEM image contrast. The imaging conditions promote strong image contrast dependence on atomic number Z . The appearing bright contrast features corresponds to the introduction of Au atoms into the Ti_3SiC_2 film. Initially Au was introduced at the top of the Ti_3SiC_2 film (at $\text{Au}/\text{Ti}_3\text{SiC}_2$ interface) while in the end (from 201 min), Au moved into the film from the right side which was the faster diffusion path because of sample geometry.

Movie caption. STEM movie showing the reaction process from Ti_3SiC_2 to Ti_3AuC_2 *in situ*.

Section S15: Electrical characteristics of the ohmic contacts over time

Figures S.13 and S.14 show the I/V curves and the corresponding electrical resistance of the $\text{IrO}_x/\text{Au}/\text{Ti}_3\text{SiC}_2/\text{SiC}$ sample over the aging experiments, respectively. As can be seen, the ohmicity of the sample remains intact over the 1000-h aging experiment, i.e., the linearity of the curves are not affected. In addition, the slope of the I/V curves increases over time; that is, the resistance decreases (after an initial run-in) during the aging experiment (Fig. S14). This decrease was also observed for the $\text{Ir}/\text{Au}/\text{Ti}_3\text{SiC}_2/\text{SiC}$ sample and is expected as the high annealing temperature, 600°C , in the absence of any oxidation or interdiffusion results in the increase of interface ordering and progress of the intercalation process, which both improve the electrical properties.

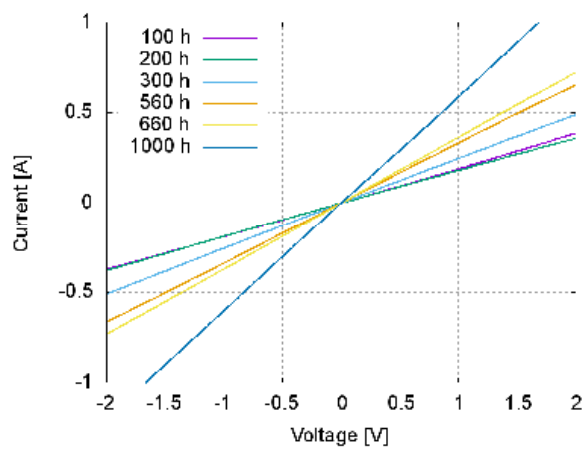


Figure S13. I/V curves for different time of annealing in 600°C air.

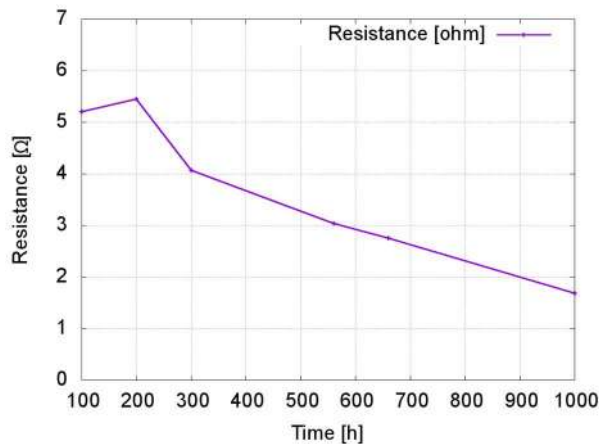


Figure S14. Resistance vs. aging time.

References

1. Blöchl, P. E. Projector augmented-wave method. *Phys. Rev. B* **50**, 17953–17979 (1994).
2. Kresse, G. & Furthmüller, J. From ultrasoft pseudopotentials to the projector augmented-wave method. *Phys. Rev. B* **59**, 1758–1775 (1999).
3. Kresse, G. & Hafner, J. Ab initio molecular dynamics for liquid metals. *Phys. Rev. B* **47**, 558–561 (1993).
4. Kresse, G. & Furthmüller, J. Efficiency of ab-initio total energy calculations for metals and semiconductors using a plane-wave basis set. *Comput. Mater. Sci.* **6**, 15–50 (1996).
5. Kresse, G. Efficient iterative schemes for ab initio total-energy calculations using a plane-wave basis set. *Phys. Rev. B* **54**, 11169–11186 (1996).
6. Perdew, J. P., Burke, K. & Ernzerhof, M. Generalized Gradient Approximation Made Simple. *Phys. Rev. Lett.* **77**, 3865–3868 (1996).
7. Hobbs, D., Kresse, G. & Hafner, J. Fully unconstrained noncollinear magnetism within the projector augmented-wave method. *Phys. Rev. B* **62**, 11556–11570 (2000).
8. Marsman, M. & Hafner, J. Broken symmetries in the crystalline and magnetic structures of γ -iron. *Phys. Rev. B* **66**, 224409 (2002).
9. Dronskowski, R. & Bloechl, P. E. Crystal orbital Hamilton populations (COHP): energy-resolved visualization of chemical bonding in solids based on density-functional calculations. *J. Phys. Chem.* **97**, 8617–8624 (1993).
10. Dahlqvist, M., Alling, B., Abrikosov, I. A. & Rosén, J. Phase stability of Ti_2AlC upon oxygen incorporation: A first-principles investigation. *Phys. Rev. B* **81**, 24111 (2010).
11. Dahlqvist, M., Alling, B. & Rosén, J. Stability trends of M A X phases from first principles. *Phys. Rev. B* **81**, 220102 (2010).
12. Deringer, V. L., Tchougréeff, A. L. & Dronskowski, R. Crystal orbital Hamilton population (COHP) analysis as projected from plane-wave basis sets. *J. Phys. Chem. A* **115**, 5461–6 (2011).
13. Maintz, S., Deringer, V. L., Tchougréeff, A. L. & Dronskowski, R. Analytic projection from plane-wave and PAW wavefunctions and application to chemical-bonding analysis in solids. *J. Comput. Chem.* **34**, 2557–67 (2013).
14. Egerton, R. F. Electron energy-loss spectroscopy in the TEM. *Reports Prog. Phys.* **72**, 16502 (2009).
15. Koski, K. J. *et al.* High-density chemical intercalation of zero-valent copper into Bi_2Se_3 nanoribbons. *J. Am. Chem. Soc.* **134**, 7584–7 (2012).
14. Duchamp, M., Xu, Q. & Dunin-Borkowski, R. E. Convenient preparation of high-quality specimens for annealing experiments in the transmission electron microscope. *Microsc. Microanal.* **20**, 1638–1645 (2014)